UBCSAND CONSTITUTIVE MODEL

Version 904aR

Documentation Report:

UBCSAND Constitutive Model on Itasca UDM Web Site

by

Michael H. Beaty, PhD, PE, GE
Beaty Engineering LLC

and

Prof. Peter M. Byrne, PhD, P.Eng.
University of British Columbia

February, 2011

Table of Contents

1 Introduction

UBCSAND is an effective stress plasticity model for use in advanced stress-deformation analyses of geotechnical structures. The model was developed primarily for sand-like soils having the potential for liquefaction under seismic loading (e.g., sands and silty sands with a relative density less than about 80%). The model predicts the shear stress-strain behavior of the soil using an assumed hyperbolic relationship, and estimates the associated volumetric response of the soil skeleton using a flow rule that is a function of the current stress ratio η. The model can be used in a fully-coupled fashion where the mechanical and groundwater flow calculations are performed simultaneously.

One of the first uses of UBCSAND was for predicting the behavior of the CANLEX (Canadian Liquefaction Experiment) embankments. The fills were rapidly constructed on loose tailing deposits to create a liquefaction response (Puebla, et al., 1997). The model was soon adapted to seismic evaluations and applied to the response analysis of the Wildlife Site and the Superstition Hills Earthquake of 1987 (Beaty and Byrne, 1998). The model continued to be refined after these early analyses.

The first version of UBCSAND that was widely used for seismic analyses was completed in 2002 and became known as UBCSAND 904a. This version has seen considerable use and scrutiny since its development, and has been used as the base version for several modified codes. One of these modifications, version 904aR, was developed during the evaluation of Success Dam in California to improve the behavior of the model under certain types of loading. Particular focus was given to the prediction of excess pore pressures when significant static shear stresses were present.

This document presents an overview of the 904a version of UBCSAND, a description of the changes made for the 904aR version, and an account of the behavior of the revised model in terms of element test simulations and the back-analyses of a case history.

2 Description of UBCSAND Version 904a

Cyclic shear strains induce plastic volume compaction in granular soils. Martin et al. (1975) presented quantitative data in their landmark paper and showed that the amount of compaction per cycle is proportional to the cyclic shear strain amplitude and accumulated volume compaction, and is independent of normal effective stress. They also showed that the pore pressure generated per cycle is dependent on the plastic volumetric strain, the rebound modulus of the soil, and the stiffness of the pore fluid.

The response of sand is controlled by the skeleton behavior. A fluid (air water mix) in the pores of the sand acts as a volumetric constraint on the skeleton if drainage is curtailed. It is this constraint that causes the pore pressure rise that can lead to liquefaction. Provided the skeleton or drained behavior is appropriately modeled under monotonic and cyclic loading conditions, and the stiffness of the pore fluid and drainage are accounted for, the liquefaction response can be predicted. This is the approach incorporated into UBCSAND.

UBCSAND is a constitutive model that directly estimates the response of the soil skeleton to general increments of loading. The response of the pore fluid is coupled to the skeleton response through the bulk modulus of the fluid. UBCSAND is based on classic plasticity theory and the characteristic sand behavior observed in laboratory tests under monotonic and cyclic loading conditions. The UBCSAND model and its uses have been documented in many papers, including those listed in Appendix 1.

2.1 Elastic Response

The elastic component of response is assumed to be isotropic and specified by a shear modulus, G^e, and a bulk modulus, B^e, as follows:

[1] $$G^e = K_G^e \cdot P_a \cdot \left(\frac{\sigma'}{P_a} \right)^{ne}$$

[2] $$B^e = \alpha \cdot G^e$$

where K_G^e is a shear modulus number that depends on the relative density and varies from about 500 for loose sand to 2000 for dense sand,

P_a is atmospheric pressure in the chosen units,

σ' is the mean stress in the plane of loading equal to $(\sigma'_x + \sigma'_y)/2$,

ne varies between 0.4 and 0.6, or approximately 0.5, and

α depends on the elastic Poisson's ratio which is in the range 0.0 ~ 0.2 (Hardin 1978) with the result that α varies between 2/3 and 4/3 or is approximately unity.

2.2 Plastic Response

Plastic strains are controlled by the yield surface and flow rule. The yield surface is represented by a radial line from the origin in stress space as shown in Figure 1. For first time shear loading, the yield surface is controlled by the current stress state, point A in Figure 1. As the shear stress increases, the stress ratio $\eta(=\tau/\sigma')$ increases and causes the stress point to move to point B. τ and σ' are the shear and normal effective stresses on the plane of maximum shear stress. The yield surface is dragged to the new location passing through point B and the origin. This results in plastic strains, both shear and volumetric. The plastic shear strain increment, $d\gamma^p$, is related to the change in shear stress ratio, $d\eta$, as shown in Figure 2 and can be expressed as

[3] $$d\gamma^p = \frac{1}{G^p/\sigma'} \cdot d\eta$$

where G^p is the plastic shear modulus and, assuming a hyperbolic relationship between η and γ^p, is given by:

[4] $$G^p = G_i^p \cdot (1 - \frac{\eta}{\eta_f} \cdot R_f)^2$$

where G_i^p is the plastic modulus at a low level of stress ratio $(\eta = 0)$,
η_f is the stress ratio at failure and equals $\sin\phi_f$,
ϕ_f is the peak friction angle, and
R_f is the failure ratio used to truncate the best fit hyperbolic relationship and prevent the over-prediction of strength at failure. R_f generally varies between 0.7 and 0.98 and decreases with increasing relative density.

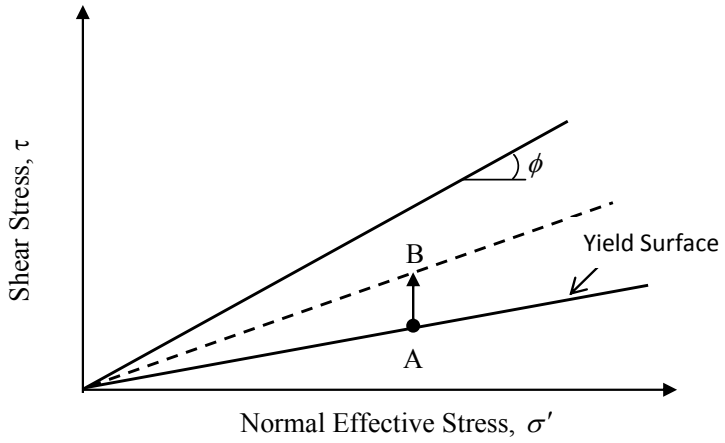

Figure 1. Yield surface in UBCSAND.

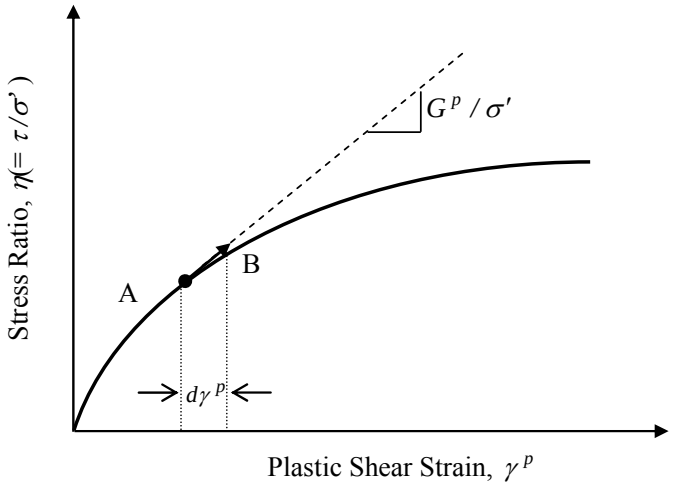

Figure 2. Plastic strain increment and plastic modulus.

The associated increment of plastic volumetric strain, $d\varepsilon_v^p$, is related to the increment of plastic shear strain, $d\gamma^p$, through the flow rule as follows:

[5] $$d\varepsilon_v^p = (\sin\phi_{cv} - \frac{\tau}{\sigma'}) \cdot d\gamma^p$$

where ϕ_{cv} is the constant volume friction angle or phase transformation angle. This flow rule can be derived from energy considerations and is similar to stress dilation theory (Rowe 1962; Matsuoka and Nakai 1977).

Yield loci and the corresponding direction of the plastic strains resulting from the flow rule are shown in Figure 3. Significant shear-induced plastic compaction occurs at low stress ratios, while no compaction is predicted at stress ratios corresponding to ϕ_{cv}. At stress ratios greater than ϕ_{cv}, shear induced plastic expansion or dilation is predicted. This simple flow rule is in close agreement with the characteristic behavior of sand observed in laboratory element testing. Upon unloading, defined as a reduction in the magnitude of η, the sand is assumed to behave elastically and no plastic strains are generated.

The sign of the stress ratio is controlled by the sign of the shear stress on the horizontal plane. This is a simplifying assumption but recognizes the importance of the horizontal plane in many geotechnical structures (i.e., the importance of simple shear loading). Both positive and negative values of the maximum stress ratio are separately tracked. This allows the plastic behavior to include aspects of both kinematic and isotropic hardening.

The plastic shear modulus discussed above is applicable for virgin or first time loading. Whenever the current load increment pushes the yield surface outside the previous maximum stress ratio limits, this increment of loading is considered first time loading. When an increment of loading occurs within the previous maximum stress ratio limits, the sand is assumed to behave plastically but with a plastic modulus that is several times stiffer than for first time loading. The maximum stress ratio limits are defined as the largest positive and negative values of η that have occurred since the start of loading.

Not all loading increments generate plastic strains in version 904a. Unloading occurs when there is a decrease in the magnitude of the stress ratio. If the stress ratio should then begin to increase in magnitude before there has been a change in the sign of the stress ratio, then this increment of loading is considered a reloading increment. Reloading increments are assumed to respond elastically with no plastic shear or volumetric strains. Reloading occurs until the stress ratio equals the previous maximum stress ratio that occurred during the current loading cycle. Once this stress ratio has been achieved, subsequent loading increments generate plastic strains This definition of reloading is shown schematically on Figure 4.

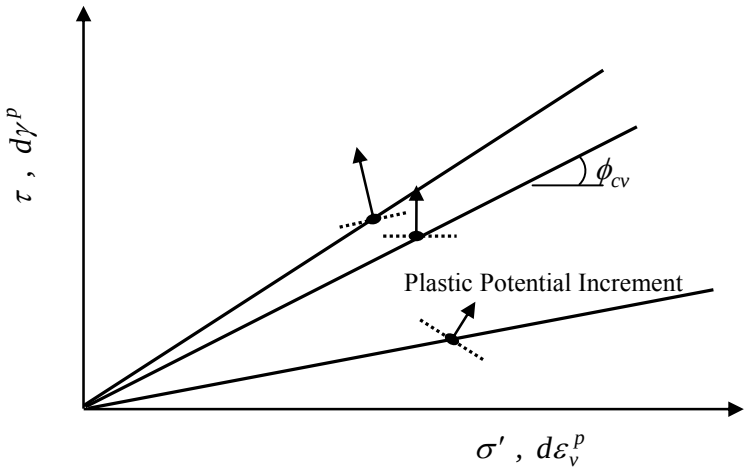

Figure 3. Directions of plastic strains associated with location of yield surface.

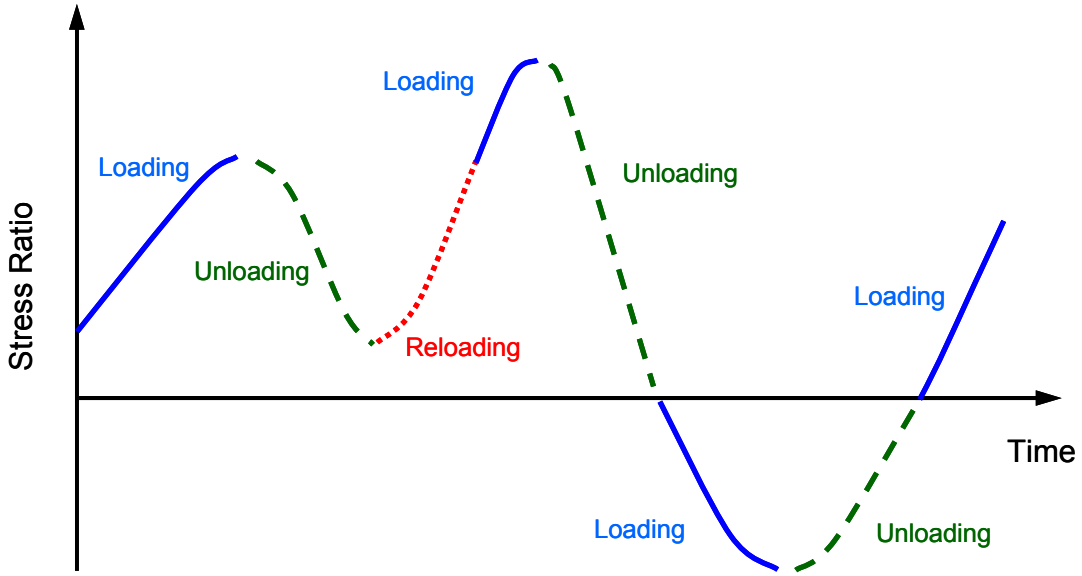

Figure 4. Stress ratio history showing loading, unloading, and reloading.

3 Description of UBCSAND Version 904aR

Revisions to version 904a were prompted by analyses of Success Dam in California. The selection of an appropriate constitutive model for these analyses followed a rigorous evaluation made by the Sacramento District Office of the Army Corps of Engineers. This evaluation process benefited from the general guidance and input of the advisory panel for the Success Dam project. It also led to several changes to the constitutive model.

Preliminary analyses of Success Dam using the 904a version of UBCSAND showed a significantly smaller zone of high excess pore pressure beneath the upstream shell of the dam than was anticipated. Concerns regarding the extent of predicted high pore pressures were supported by several independent evaluations: 1) estimates of pore pressure generation based on results from Quad4 analyses, 2) estimates of pore pressure generation from a cycle-counting FLAC model developed by URS, and 3) and an examination of shear stress histories predicted by the UBCSAND model in key elements. The initial static shear stress, or static bias, was found to have an unexpected influence on the generation of excess pore pressure.

Version 904a includes the simplifying assumption that cycles of partial unloading and reloading are elastic. These cycles are defined as ones where the shear stress drops and then increases but there is no reversal in the direction of the shear stress. For many locations beneath the upstream shell of Success Dam, the initial static shear stress is larger than the magnitude of most cyclic loading cycles. In other words, many of the larger shear stress cycles were considered partial unload-reload cycles and did not contribute to the excess pore pressure. An example shear stress history computed for Success Dam beneath the upstream shell is shown in Figure 5.

UBCSAND was modified to improve response predictions for cases with significant static bias. This was accomplished using published relationships between cyclic strength ratio and static bias as a guide. Although the effect of static bias on liquefaction resistance is somewhat uncertain, it is typically addressed in simplified procedures through a factor termed K_α. Two relationships for K_α were proposed by Harder and Boulanger (1997) and Idriss and Boulanger (2003). These relationships were based on a limited set of simple shear test results which were considered to provide the most reliable data. These plots represent the current state of practice for the evaluation of slopes and embankments.

The modifications to UBCSAND for version 904aR were governed by two criteria:

1. capture the general trends incorporated into the K_α plots, and
2. limit changes to the structure, assumptions, input parameters, and behavior of the 904a version.

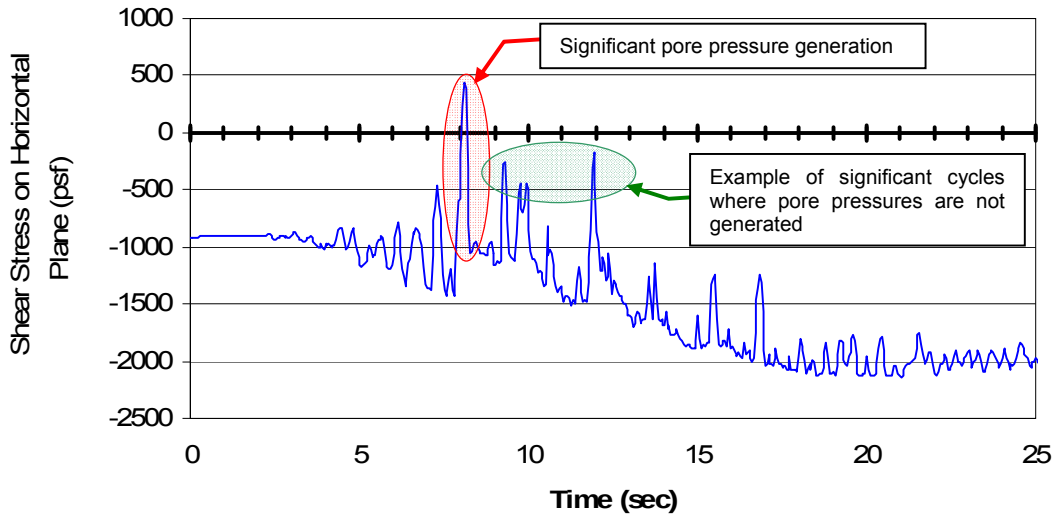

Figure 5. Example of predicted shear stress beneath upstream shell of Success Dam using UBCSAND version 904a.

The primary changes made to UBCSAND are summarized below:

1. *Partial unload-reload cycles generate plastic volumetric strains*

   In version 904a, the location of the yield surface is not modified when an element unloads until a shear stress reversal occurs. For partial unload-reload cycles (i.e., no stress reversal), the response is entirely elastic until the stress state once again reaches the yield surface. For version 904a, no plastic volumetric strains are generated during these partial unload-reload cycles.

   In version 904aR, the location of the yield surface is now modified during increments of unloading. The yield surface systematically drops as the magnitude of the mobilized stress ratio η decreases. The yield surface lags slightly behind the decreasing stress state so that a small elastic zone separates the stress state and the yield surface. Adjusting the yield surface in this way allows for the generation of plastic volumetric strains when the element is reloaded even if a stress reversal has not occurred. The generation of pore pressures during partial unload-reload cycles is supported by laboratory testing, such as the data discussed in Section 4.9.

   The plastic shear stiffness associated with reloading is controlled by the internal variable m_urstif, which directly factors the plastic shear modulus. This factor

was needed in order to reasonably predict the behavior shown in the K_α charts. The K_α factor relates the cyclic resistance with no static shear bias ($\alpha = 0$) to the cyclic resistance at a static bias of α. The static bias α is defined as the initial shear stress on the x-y plane divided by the initial vertical effective stress.

The magnitude of m_urstif is a function of the relative change in η. m_urstif is equal to a minimum of 1.0 at the instant of a stress reversal and smoothly increases to a relatively large factor for small unloading cycles. The relationship used to define m_urstif was developed by matching model predictions to expected K_α behavior using direct simple shear (DSS) simulations.

2. *Plastic shear stiffness modified for non-symmetric loading cycles*

In versions 904a and 904aR, no plastic strains are generated during increments of unloading (i.e., decreasing stress ratio η). Any plastic strains that should occur during unloading are assumed to be accounted for during the subsequent loading cycle after a shear stress reversal. In other words, the actual plastic behavior can be approximated if the plastic shear modulus during loading is made somewhat softer. This will induce additional plastic strains during loading to account for any strains that were missed during the unloading increments. This approximation is generally reasonable, although it did produce some undesirable trends in the predicted K_α behavior. The primary motivation for this modification was to smooth the predicted relationship between static bias and liquefaction resistance.

The plastic shear stiffness is now modified to account for the effects of non-symmetry. Symmetry is evaluated at stress reversals by computing the ratio of the peak stress ratio η from the previous two half-cycles of loading (i.e., $\eta_{ratio\_k} = \eta_{peak\_k-1} / \eta_{peak\_k-2}$). If $\eta_{ratio\_k} \geq 1$ then the previous full cycle of loading is considered to be similar to a symmetric load cycle and the plastic shear stiffness is not adjusted. If $\eta_{ratio\_k} < 1$ then the load cycle is considered non-symmetric and the plastic shear modulus is stiffened using the internal parameter m_sym. The adjustment factor m_sym ranges between 1.0 for symmetric cycles to a maximum of 1.3 to 1.9 for highly non-symmetric cycles. This definition for symmetry is illustrated in Figure 6.

3. *Post-dilation softener made a function of accumulated dilative strains*

Plastic dilative strains are used by UBCSAND to identify elements that will experience significant plastic volumetric contraction upon a shear stress reversal. This plastic volumetric contraction is induced in the model by significantly softening the plastic shear modulus after a stress reversal. In version 904a, the required amount of softening is based solely on the plastic dilative strain

experienced during the previous half cycle. This was revised in version 904aR so that the magnitude of softening is based on the accumulated amount of plastic dilation that the element has experienced since the start of loading. This dilation is accumulated only when the stress ratio is close to the maximum allowed stress ratio (i.e., m_ratf).

This revised definition assumes that plastic dilative strains cause the soil skeleton to soften, and that this damage to the skeleton endures beyond the current load cycle. This change in defining the softener allows for a more gradual transition into liquefied behavior. This was particularly important for simulating the response of denser sands under a static bias.

The post-dilation softener is a function of both the loading symmetry and the accumulated dilative strains. The internal parameters m_symdil and m_dilsft address these two aspects. The functional relationships for these factors were derived through DSS simulations and comparison to expected liquefaction triggering and K_α behavior.

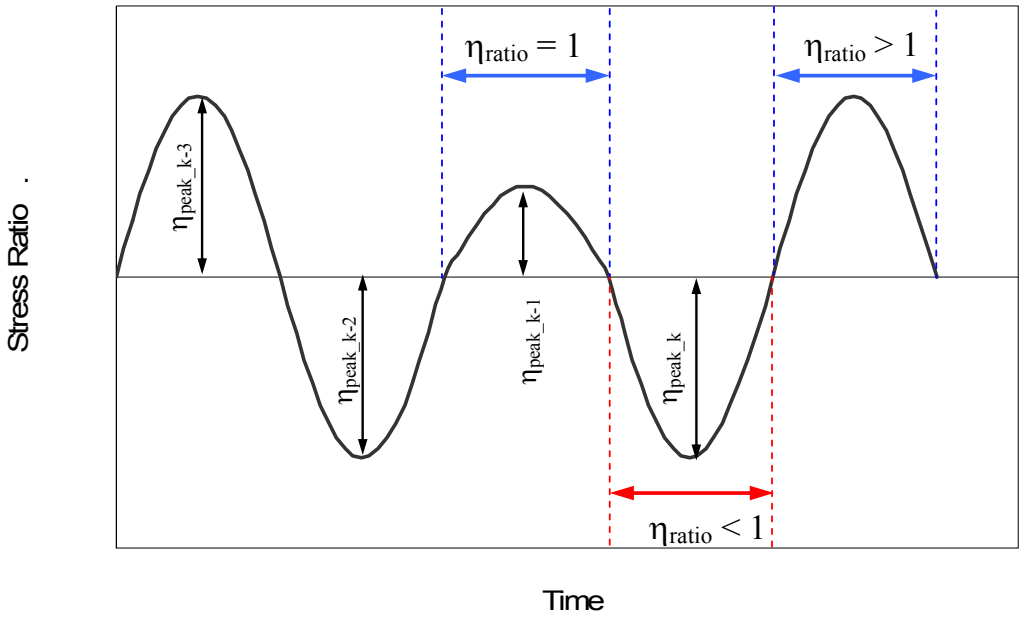

Note: $\eta_{ratio} \geq 1$: previous full cycle considered symmetric.
$\eta_{ratio} < 1$: previous full cycle considered non-symmetric.

Figure 6. Illustration of symmetric and non-symmetric loading cycles.

4. *Smooth transition between primary and secondary yield surfaces*

   UBCSAND uses two yield surfaces to incorporate plastic response during loading. The primarily yield surface is active for conditions of virgin or primary loading. Primary loading is defined as an increase in stress ratio above the previous maximum stress ratio experienced by the element. The occurrence of primary loading is evaluated separately in both the positive and negative loading directions. In contrast to primary loading, a secondary yield surface is used when loading increments occur below the previous maximum stress ratio.

   In version 904a, an abrupt change in response can occur when the model switches from the secondary to the primary yield surface. These abrupt changes are most noticeable in plots of stress path. Versions 904aR includes a transition between these two yield surfaces. As the current stress ratio approach the previous maximum stress ratio, the properties of the yield surface begin to interpolate between those of the secondary and primary surfaces. The benefit of this transition is to produce somewhat smoother stress path behavior, although the overall effect on model response is expected to be minor.

5. *Revised relationships for R_f and ϕ_f*

   Two adjustments were made to the generic input parameters. The friction angle at failure, m_phif, was increased for sands with $(N_1)_{60}$ greater than 15. For example, the value of m_phif for $(N_1)_{60}$=25 was increased from 35.5° to 37.5°. This change in friction angle was made in order to stiffen the post-liquefaction response of denser sands. The relationship for the hyperbolic adjustment factor, m_rf, was also revised. The current equation better represents the trend reported in Byrne et al. (1987).

6. *Calibration equations for m_hfac1*

   Version 904a included a calibration factor m_hfac1 that could be adjusted element by element. The primary use of this factor is to adjust the plastic shear stiffness with confining stress in order to achieve the anticipated relationship between initial confining stress and cyclic resistance ratio, or the K_σ effect. To reduce the amount of calibration needed on typical applications of UBCSAND, a set of generic equations was developed for m_hfac1 that are based on the current m_n160 and the initial effective stress state of each element. These equations allow for easy calculation of element-specific values of m_hfac1, provide more continuity between evaluations performed by different analysts, and simplify the development of preliminary analyses. The calibration equations for m_hfac1 assume the generic input parameters are being used for UBCSAND, and that the desired K_σ relationship is as defined by the NCEER workshop (Youd

et al, 2001). These equations for m_hfac1, provided Appendix 1, are optional and can be easily replaced by project-specific relationships.

3.1 Static analysis mode

A new parameter m_static was added to permit the model to function in a simpler manner when used during pre-earthquake static analyses. Certain aspects of the dynamic formulation are deactivated when m_static is set equal to 1: dilative volumetric strains are not accumulated; only the primary yield surface is used (for m_ocr < 2); load cycles are not counted; and the unload-reload plasticity adjustments are not included. The full seismic formulation is used when m_static=0.

4 Single Element Behavior of UBCSAND 904aR

A series of single element analyses were performed to demonstrate the behavior predicted by UBCSAND 904aR[1]. These analyses were constructed to simulate an idealized DSS laboratory test: the two base nodes are fixed against translation and the two top nodes are constrained so that their movements are identical. Loading is imposed by applying a horizontal velocity to the top nodes. The vertical movement of the top nodes is not externally fixed. The porosity of the element was assumed to be 0.5, while the bulk modulus of the pore fluid was taken to be one-fourth the value of de-aired water, or K_w = 5e6 kPa. The generic input parameters provided in Appendix 2 were used in the analyses.

For the sake of making comparisons between the UBCSAND liquefaction response and various empirical and laboratory relationships, a clear definition is needed for defining the onset of liquefaction in the UBCSAND element. Liquefaction is assumed to occur when either of the following two criteria is satisfied: the excess pore pressure ratio r_u exceeds 0.85 or the maximum shear strain γ exceeds 3%. r_u is a measure of the increase in pore pressure where r_u equals 0 if the pore pressures do not change, and r_u equals 1 when effective stress become equal to zero (see Section 5.1). These two criteria are similar to those often used to define the onset of liquefaction in a laboratory test. The r_u criterion was often the critical criterion for analyses using lower values of $(N_1)_{60cs}$, while the shear strain criterion was often satisfied for cases with larger $(N_1)_{60cs}$ values where a significant static bias was present.

4.1 Typical stress-strain and stress path behavior

Typical behavior of the UBCSAND model is shown in Figure 7 to Figure 10. Monotonic and cyclic DSS simulations, both drained and undrained, were performed for two density states: $(N_1)_{60}$ = 5 and 15. All the simulations were performed using an initial effective vertical stress of 100 kPa. Initial K_o conditions of 0.5 and 1.0 were evaluated for each value of $(N_1)_{60}$. The analyses used the generic input parameters described in Appendix 2.

These figures are intended to demonstrate the typical behavior of UBCSAND in a simple shear simulation. A direct comparison to laboratory tests results is shown Section 4.9.

The drained monotonic predictions are shown in Figure 7. The denser material is seen to have a stiffer stress-strain response, with dilative volumetric strains after a shear strain of about 0.3%. The $(N_1)_{60}$ = 5 test shows a small dilative response after shear strains of

[1] The results and description of UBCSAND 904aR presented in the report refer to the constitutive code version UBCSAND904aRDP.dr8.

about 2.5%. For both cases, the $K_o = 0.5$ response is stiffer than the $K_o = 1.0$ response, although the effect is more pronounced on the looser sand.

The corresponding undrained response is shown on Figure 8. As expected, the $(N_1)_{60} = 15$ sand shows significantly stiffer and stronger behavior than the $(N_1)_{60} = 5$ sand. For the $(N_1)_{60} = 5$ sand, the $K_o = 1.0$ response is significantly softer than the $K_o = 0.5$ analysis. This trend is reversed for the $(N_1)_{60} = 15$ sand, which is consistent with the observations discussed in Section 4.7.

Figure 9 shows predictions for drained cyclic loading, while Figure 10 shows predictions for undrained cyclic loading. The applied cyclic loading in each case was equal to the CRR_{15} as determined from the NCEER/NSF chart. For the drained case, 15 cycles of this loading were applied. The trends observed from the cyclic loading are reasonable, although UBCSAND is still shown to be sensitive to the initial K_o conditions. The potential importance of K_o on the liquefiability of an element is seen most clearly in the predictions for $(N_1)_{60} = 5$: the volumetric strain versus shear strain plot for drained conditions (Figure 9c) and the stress path plot for undrained conditions (Figure 10c). The cyclic analysis results are consistent with the monotonic loading predictions.

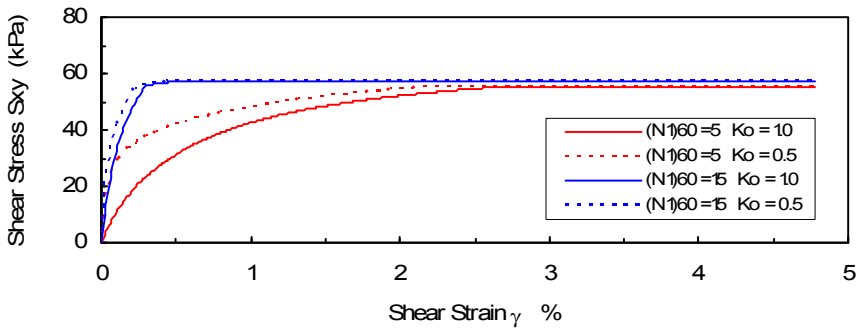

a. Stress-strain

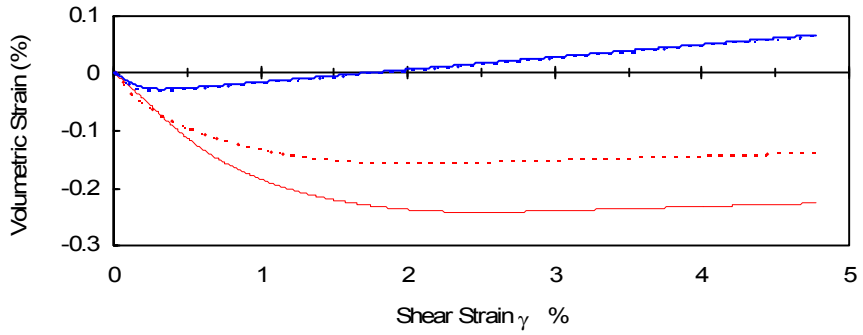

b. Volumetric strain versus shear strain

Figure 7. UBCSAND 904aR predictions of monotonic drained loading.

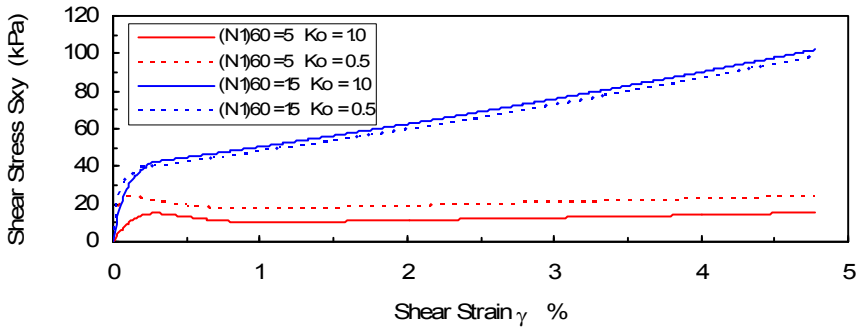

a. Stress-strain

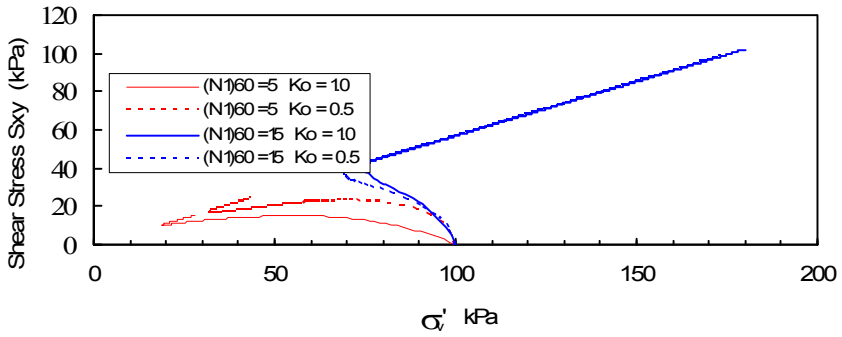

b. Stress path

Figure 8. UBCSAND 904aR predictions of monotonic undrained loading.

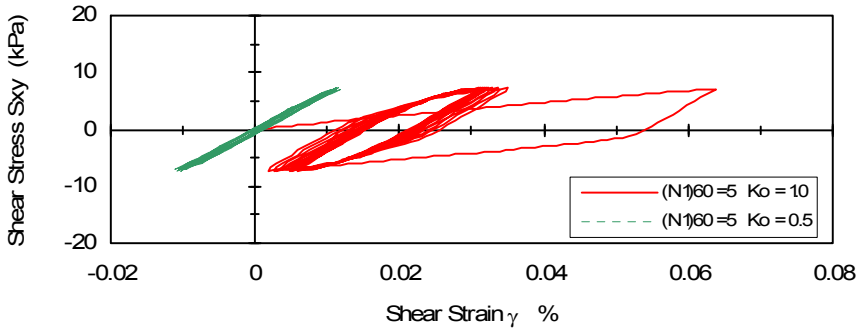

a. Stress-strain for $(N_1)_{60} = 5$

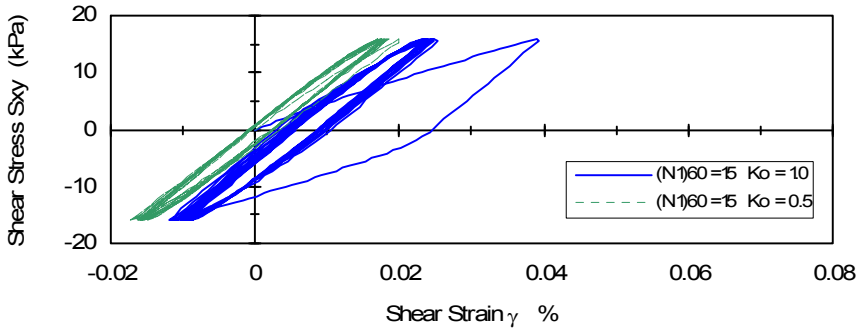

b. Stress-strain for $(N_1)_{60} = 15$

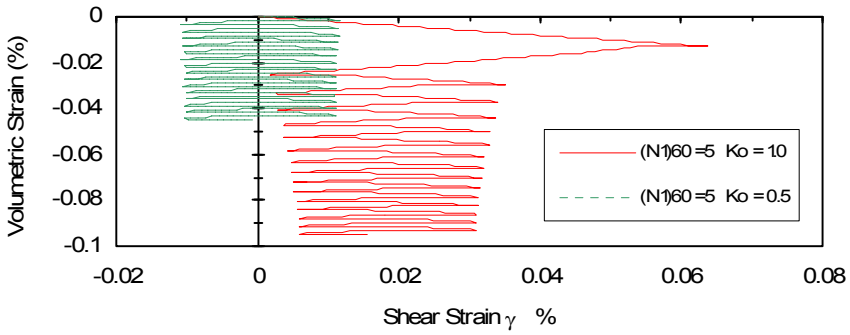

c. Volumetric strain versus shear strain for $(N_1)_{60} = 5$

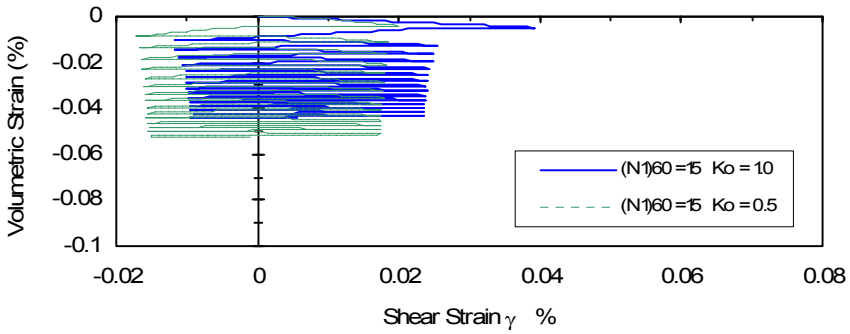

d. Volumetric strain versus shear strain for $(N_1)_{60} = 15$

Figure 9. UBCSAND 904aR predictions of drained cyclic loading.

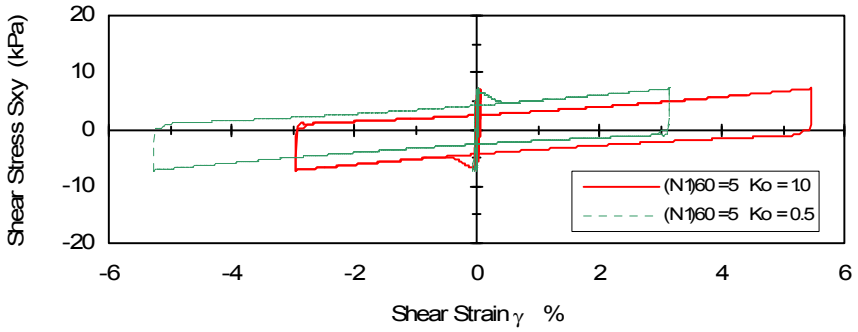

a. Stress-strain for $(N_1)_{60}$ = 5

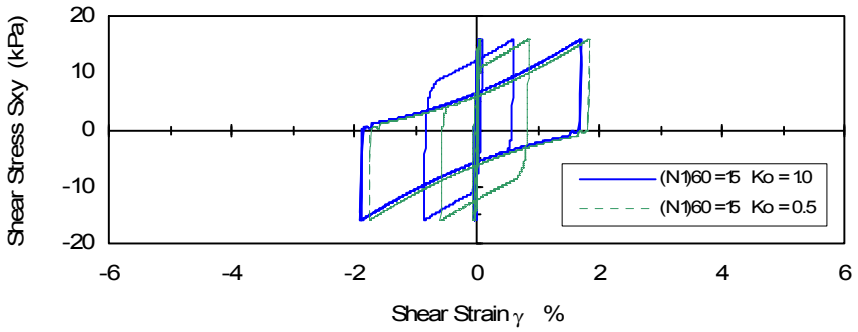

b. Stress-strain for $(N_1)_{60}$ = 15

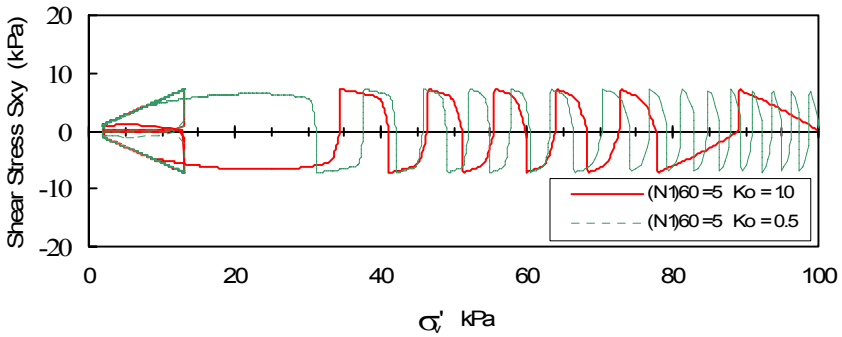

c. Stress path for $(N_1)_{60}$ = 5

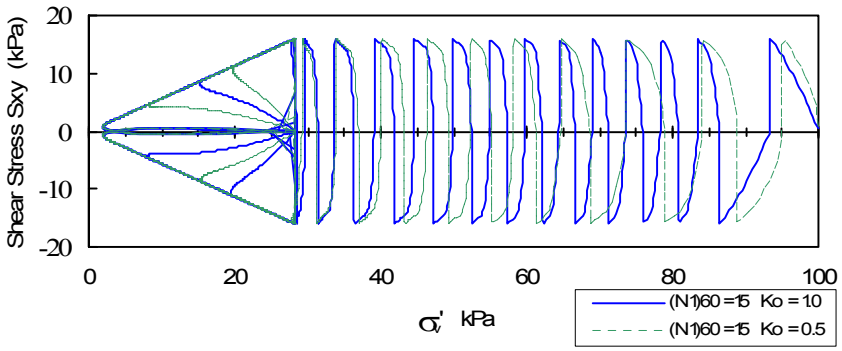

d. Stress path for $(N_1)_{60}$ = 15

Figure 10. UBCSAND 904aR predictions of undrained cyclic loading.

4.2 Cyclic strength curve

The generic input parameters Appendix 2 were calibrated to reproduce the liquefaction triggering behavior recommended by the 1997 NCEER/NSF workshop (Youd et al., 2001). This was done by recognizing that the NCEER/NSF triggering chart corresponds to earthquakes with magnitudes of about 7.5. The cyclic shear stress history induced by earthquakes of this magnitude can be approximated by 15 uniform cycles of shear stress with a magnitude equal to the cyclic shear stress determined from the triggering chart. In other words, the cyclic resistance ratio indicated by the NCEER/NSF curve for a given corrected SPT blowcount, or $(N_1)_{60cs}$, should just induce liquefaction in an element if it is applied in 15 uniform cycles.

There is some uncertainty when applying the NCEER/NSF triggering curve in an advanced analysis. Typical 2-D analyses consider only a single horizontal and vertical direction of loading. Cyclic loading in the out-of-plane direction should typically increase the generation of pore pressures in an element. The data represented by the NCEER/NSF curve was obtained or estimated from actual field response and is affected by loading in three component directions. Using the NCEER/NSF curve may somewhat address the limitations of a 2-D analysis in terms of input loading, but in an uncertain manner. There is also the question of bias in the NCEER/NSF triggering relationship, caused by both the distribution of the field data in terms of initial effective stress and by the simplified analysis techniques used to develop the field estimates of cyclic stress ratio. However, these types of uncertainties are inherent in many modern analyses based on the NCEER/NSF curve.

The results of the UBCSAND simulation are shown in Figure 11. This figure shows the cyclic stress ratio causing liquefaction in 15 uniform cycles versus $(N_1)_{60}$. Each of the plotted values of cyclic resistance ratio (CRR) reflect the higher value determined from two analyses: one with K_o equal to 0.5 and the second with K_o equal to 1.0, where K_o is the ratio of horizontal effective stress to vertical effective stress at the start of loading. A discussion of the influence of K_o on the triggering resistance of UBCSAND is provided in Section 4.7.

The CRR predicted by UBCSAND is seen to increase gradually and smoothly with increasing $(N_1)_{60cs}$. A direct comparison of the CRR estimates from UBCSAND is made to several current triggering curves: the NCEER/NSF triggering curve, the curve proposed by Idriss and Boulanger (2006), and the curves proposed by Cetin et al. (2004) for a probability of liquefaction equal to 20% and 50%. The CRR estimates generated by UBCSAND are seen to agree closely with NCEER/NSF and the Idriss and Boulanger relationships. The two curves developed from the Cetin et al. (2004) approach are substantially lower.

4.3 Weighting curve

Weighting curves show the relative importance of stress cycles having different magnitudes. It takes fewer cycles of a large shear stress to liquefy a sand as compared to a small shear stress, and this relationship is reflected in the weighting curve. Weighting curves are developed in the laboratory by testing a series of equivalent sand samples with uniform cycles of cyclic loading. Each sample is tested at a different magnitude of cyclic shear stress and the corresponding number of cycles to induce liquefaction is recorded. The resulting data is plotted to produce a weighting curve, generally shown as CSR versus the log of the number of cycles to liquefaction. It is convenient to plot the CSR data in a normalized fashion, where each CSR value is divided by CSR_{15}, which is the CSR causing liquefaction in 15 cycles.

A large number of weighting curve tests performed on samples obtained by in situ freezing were compiled by Beaty (2001). These data suggest the shape of the normalized weighting curve is fairly consistent over a range of sands, while the curves

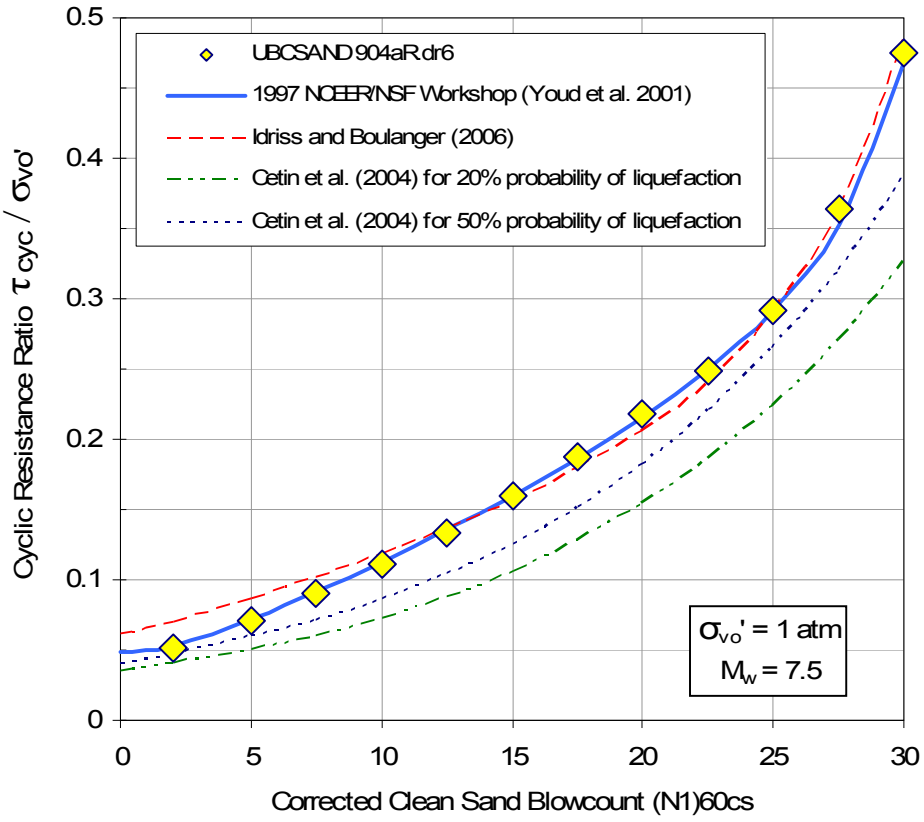

Figure 11. Values of CRR predicted by UBCSAND 904aR and compared to semi-empirical relationships.

for denser sands tended to be somewhat steeper than for looser sands. The data also suggests that the steepness of the weighting curve can be affected by the criteria used to define the onset of liquefaction.

Weighting curves were generated by UBCSAND by performing a similar series of cyclic DSS simulations. The tests were performed for a range of relative densities and the computed values are plotted on Figure 12. For comparison, the weighting curve inherent in the magnitude correction relationship proposed by Idriss and Boulanger (2006) is also shown. This curve was developed from the values of Km proposed by Idriss and Boulanger in combination with the corresponding cycles of significant loading assigned to each earthquake magnitude. The weighting curves generated by UBCSAND are in reasonable agreement with the curve developed from Idriss and Boulanger (2006). The weighting curves generally become steeper as the $(N_1)_{60}$ values increase, except for the curve estimated for $(N_1)_{60}$ = 2 which plots steeper than expected based on the other curves.

The effect of initial confining stress on the weighting curve was evaluated as shown in Figure 13. The weighting curves predicted by UBCSAND are affected by this change in confining stress, but to a relatively modest degree. The expected relationship between weighting curve and effective stress is not known.

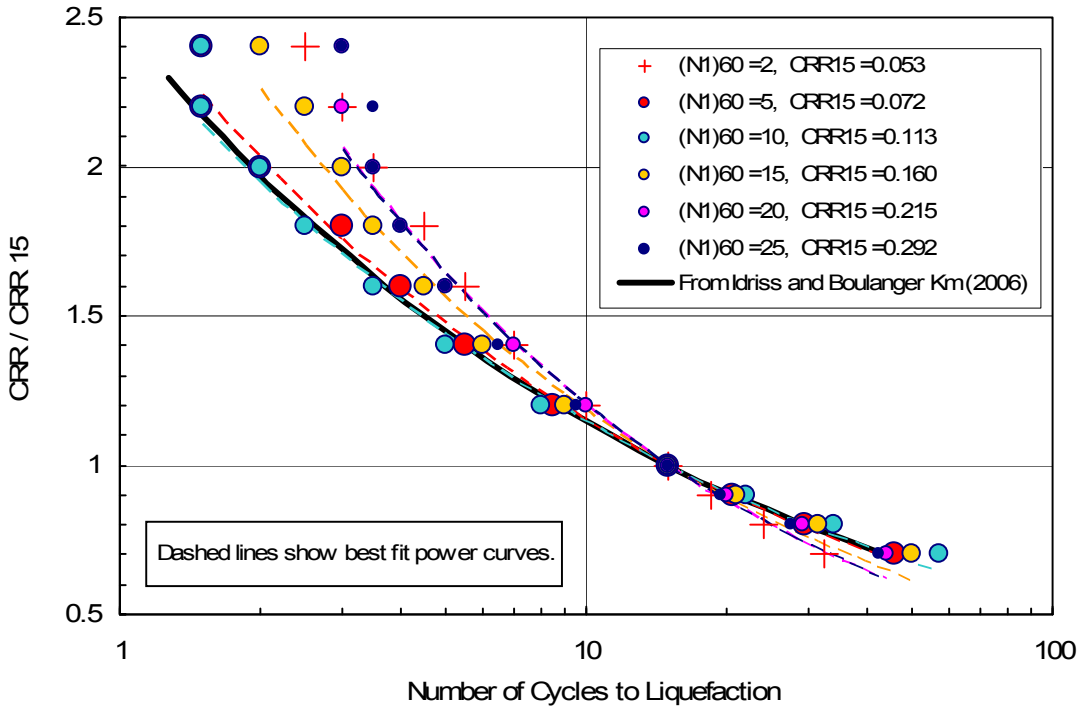

Figure 12. Cyclic strength curve for UBCSAND 904aR for σ'_{vo} = 1 atm.

4.4 Effect of initial static shear stress

The effect of the initial static shear bias on the cyclic behavior of a sand has typically been evaluated through cyclic element tests. Uniform cycles of shear load are applied to a sample of the sand, and the magnitude of the cyclic stress ratio to cause liquefaction in a set number of cycles is determined. This is repeated for various levels of initial shear stress. This initial shear stress produces a constant bias in the cyclic shear load as shown in Figure 14. The magnitude of the initial shear stress is typically expressed as α, which is the initial shear stress normalized by the initial vertical effective stress.

Changing the static shear stress will influence the cyclic resistance ratio CRR. In a simplified liquefaction triggering analysis, the correction factor K_α is defined as the CRR for a static bias of α divided by the CRR when α equals zero (i.e., $K_\alpha = CRR_\alpha / CRR_{\alpha=0}$).

A recent evaluation was made by Idriss and Boulanger (2003) of a limited number of cyclic simple shear tests performed to investigate K_α. This tests evaluated a range of relative densities and initial shear stress conditions, including those having no shear stress reversal on the horizontal plane. These tests were evaluated in terms of the relative state parameter concept, and a relationship between α, $(N_1)_{60}$, sand grain type,

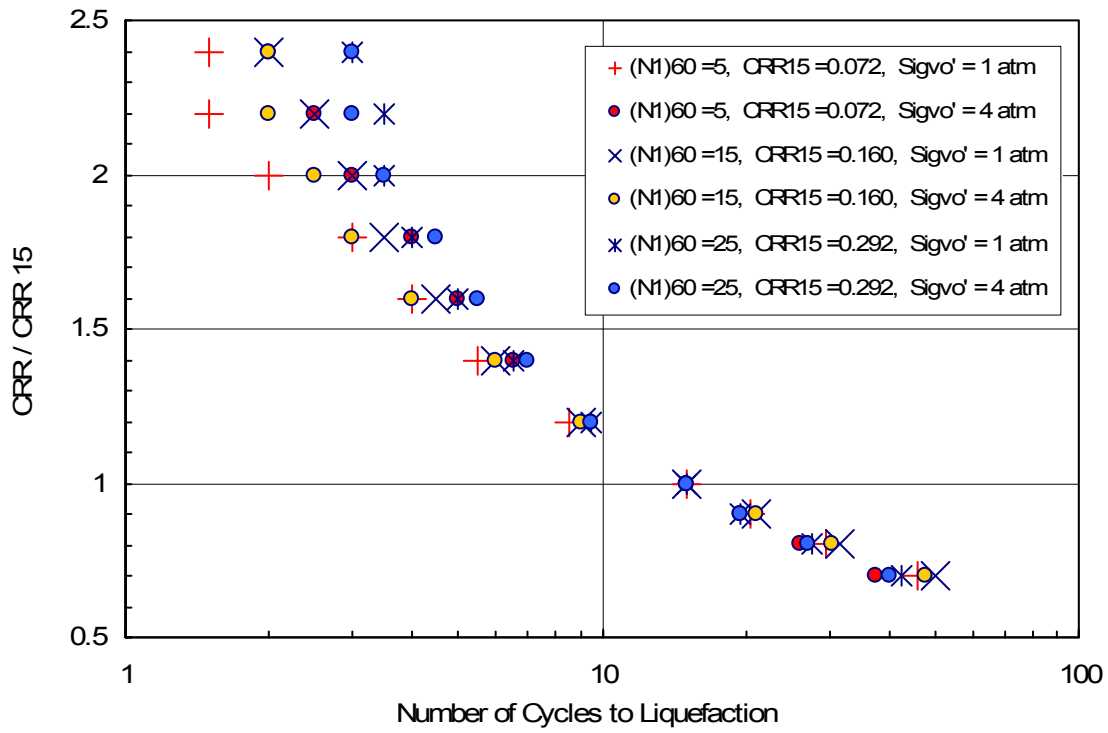

Figure 13. Weighting curves from UBCSAND 904aR for σ'_{vo} = 1 atm and 4 atm.

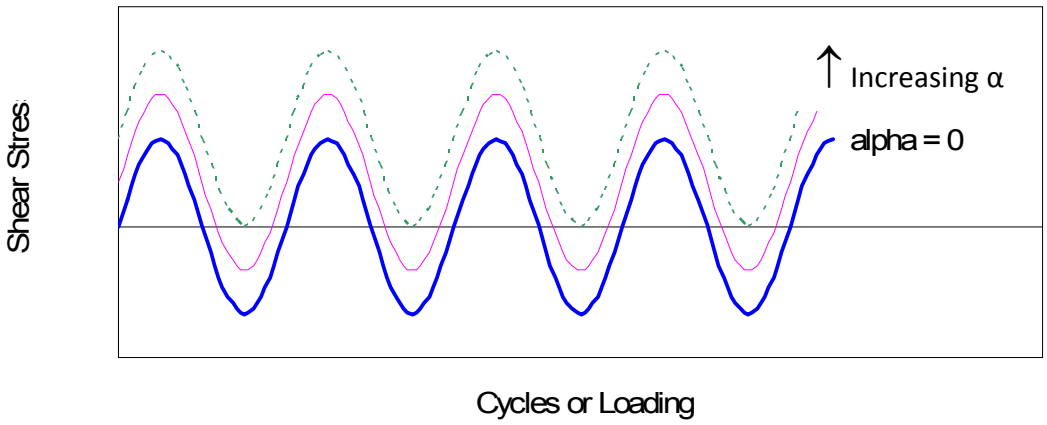

Figure 14. Example showing effect of static bias on uniform load cycles with same CSR.

effective stress, and K_α was proposed. The recommended relationship for quartz sands is shown in Figure 15 and compared against the original laboratory test data. Figure 16 shows the earlier K_α relationship by Harder and Boulanger (1997) that was presented at the 1997 NCEER workshop.

The relationship between α, $(N_1)_{60}$, and CRR was predicted by the UBCSAND model by simulating a series of cyclic simple shear tests. All of these simulations were performed using an initial σ'_{vo} = 1 atm. The CSR required to trigger liquefaction in 15 cycles was determined for each combination of α and $(N_1)_{60}$. Figure 17 compares the K_α predictions for UBCSAND 904a and UBCSAND 904aR.

The K_α behavior inherent in UBCSAND 904a deviates significantly from the K_α relationship derived from laboratory test data. The value of K_α initially drops below 1.0 for low values of α regardless of $(N_1)_{60}$. K_α eventually increases in a fairly abrupt manner as α increases. This increase occurs consistently across the range of evaluated $(N_1)_{60}$. It is more abrupt and occurs at lower values of α for low values of $(N_1)_{60}$. This behavior is not realistic when compared to the laboratory test data, and is related to the simplified response of partial unload-reload cycles.

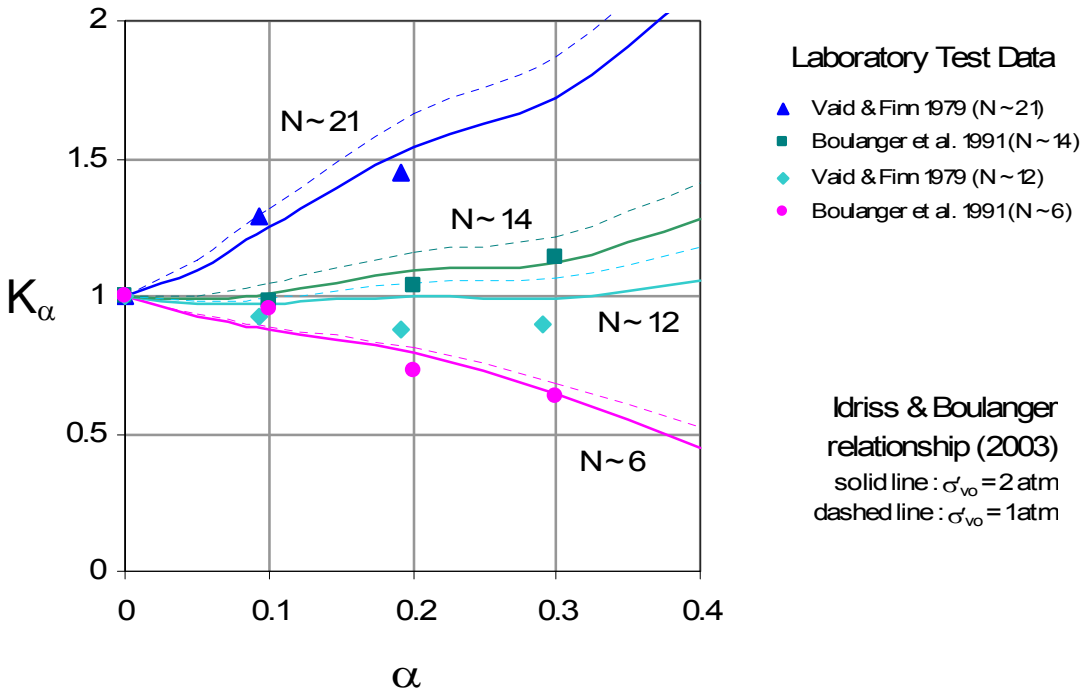

Figure 15. Relationship between K_α, α and $(N_1)_{60}$. Data and plotted trends from Idriss and Boulanger (2003). Laboratory data from tests performed at σ'_{vo} = 2 atm.

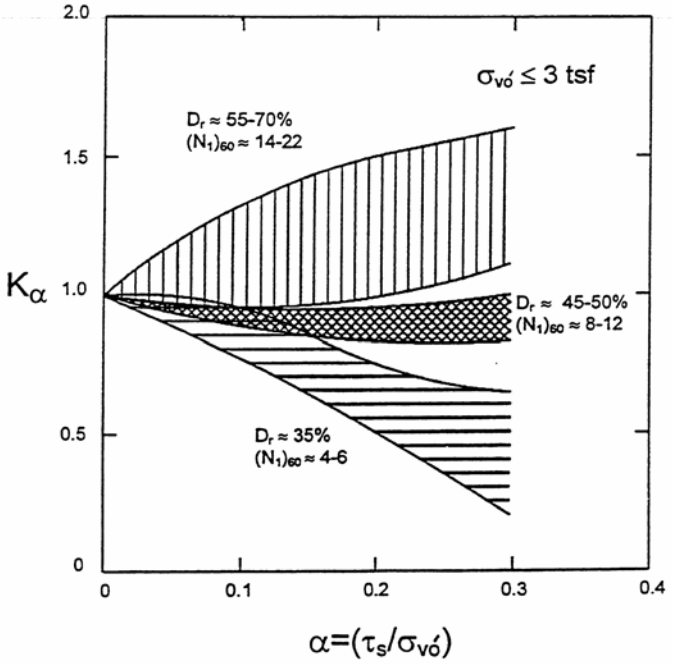

Figure 16. K_α relationship from Harder and Boulanger (1997).

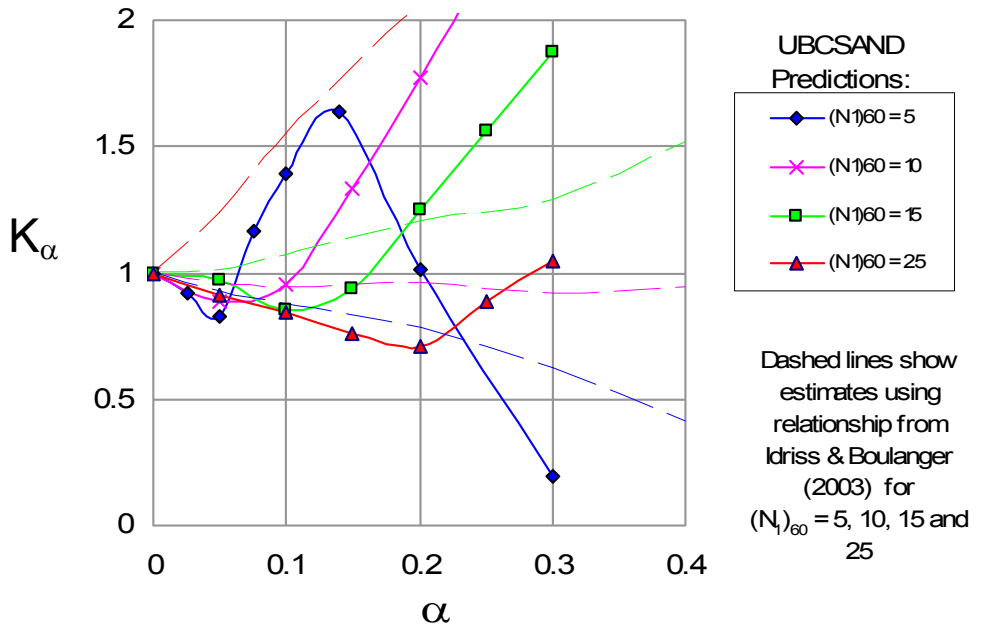

a) Predictions of UBCSAND 904a

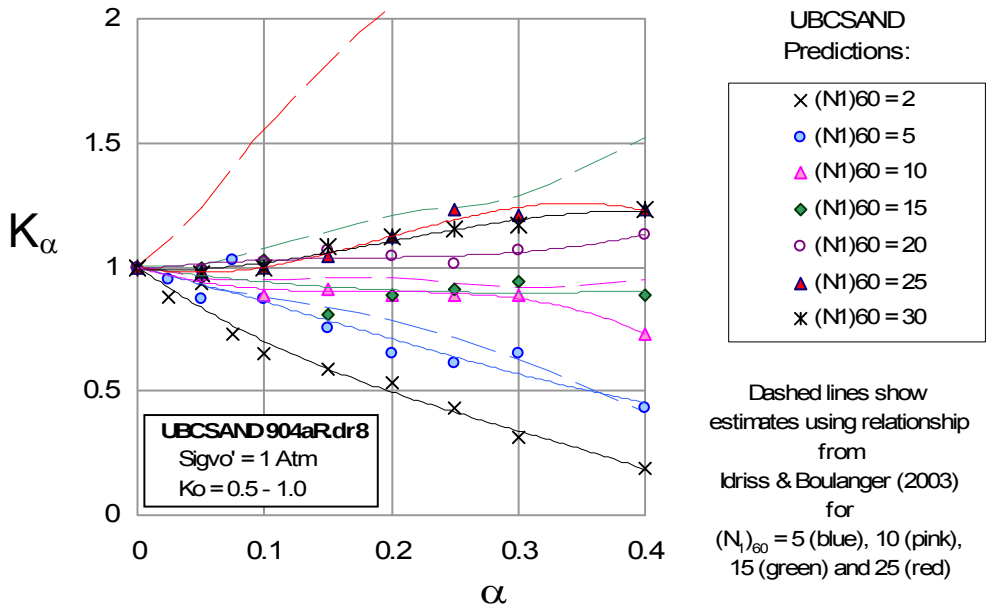

b) Predictions of UBCSAND 904aR

Figure 17. UBCSAND predictions of K_α versus relationships proposed by Idriss and Boulanger (2003).

A second feature of the K_α predictions from version 904a is the eventual decrease of K_α for $(N_1)_{60} = 5$ at $\alpha > 0.15$. This occurs due to the combination of a large static shear stress and the initial pulse of the cyclic load. This initial pulse induces strain softening and causes the element to fail under a monotonic load. The shear strains resulting from this monotonic load are significant and satisfy the liquefaction triggering criteria.

An improved relationship between α, $(N_1)_{60}$, CSR, and liquefaction resistance is seen in the K_α predictions for UBCSAND 904aR shown on Figure 17 (b) and Figure 18. The objectives of 904aR were to eliminate the artificial increase in the predicted values of K_α with increasing α, to create consistency between the predicted K_α curves so that larger values of K_α would occur for larger values of $(N_1)_{60}$ over the full range of α, and to generally produce K_α estimates that were approximately equal or somewhat less than those suggested by the data and relationships presented by Idriss and Boulanger (2003). A further restraint was imposed to prevent the model from predicting K_α values significantly larger than 1. This constraint reflects the uncertainty regarding the effect of static bias in field situation, including how out-of-plane motions will affect pore pressure generation beneath slopes. Most of these objectives were achieved in 904aR.

4.5 Modulus reduction and damping behavior

The relationship between secant modulus, hysteretic damping, and the magnitude of

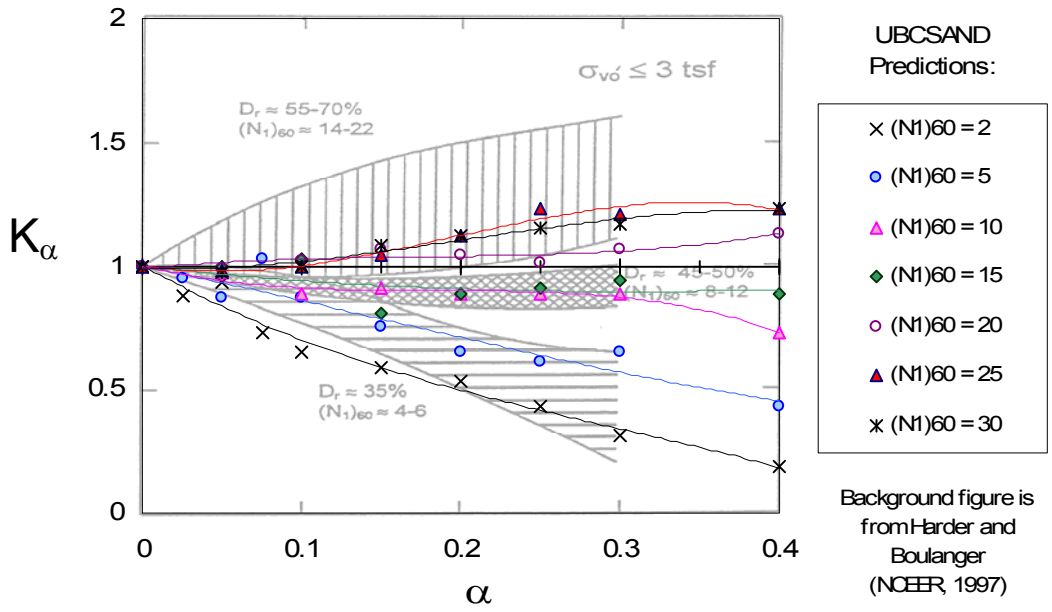

Figure 18. Comparison of K_α from UBCSAND 904aR versus Harder and Boulanger (1997).

shear strain cycles was evaluated for UBCSAND and compared to typical relationships. DSS tests were performed using UBCSAND with the generic input parameters. The analyses assumed drained conditions and were performed with an initial σ'_{vo} of 1 atm. Initial stress states of K_o = 0.5 and K_o = 1.0 were evaluated. The cyclic loading was applied in a strain-controlled and symmetric manner. Four cycles of loading were applied at each selected value of strain, and the average secant modulus and damping were determined from the 4th computed cycle. Figure 19 shows the curves estimated for $(N_1)_{60}$ values of 10 and 20.

The reduction in shear stiffness with strain that is predicted by UBCSAND is seen to be in reasonable agreement with the Idriss (1999) trend for sand. The amount of damping predicted by the model for symmetric load cycles is seen to be significantly higher than anticipated from soil tests. For example, the anticipated damping at a cyclic shear strain of 0.1% is approximately 10% to 20% of critical damping. The damping produced by UBCSAND at this strain level is approximately 30% for the two sands that were simulated. The minimum damping produced by UBCSAND for symmetric loading at small strains ranges from near 0% to 10%. The larger than anticipated damping produced by UBCSAND is due in large part to the simplification of elastic unloading at the maximum shear modulus G_{max}. The use of linear elastic unloading creates an extended stiff portion to the stress-strain curve, producing larger loop areas than would be anticipated from a laboratory test.

A significant difference is seen between the K_o = 0.5 and K_o = 1.0 analyses at small strain levels. This difference is caused by the tendency for the elastic response to dominate for the K_o=0.5 analysis until the direction of the peak shear stress sufficiently rotates.

The large damping inherent in the UBCSAND model occurs for symmetric load cycles. A somewhat reduced damping is anticipated for cycles that are non-symmetric. For example, samples that partially unload and then reload with a stiffened shear modulus should dissipate a relatively small amount of energy through hysteresis during the unload-reload cycle.

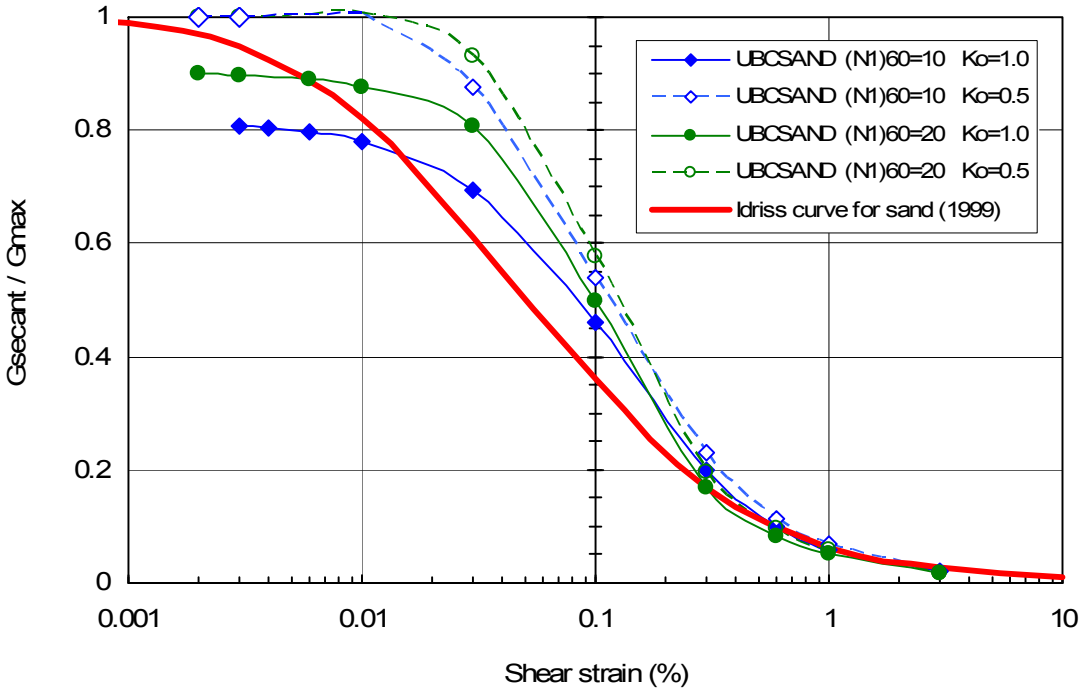

a) Modulus reduction curves.

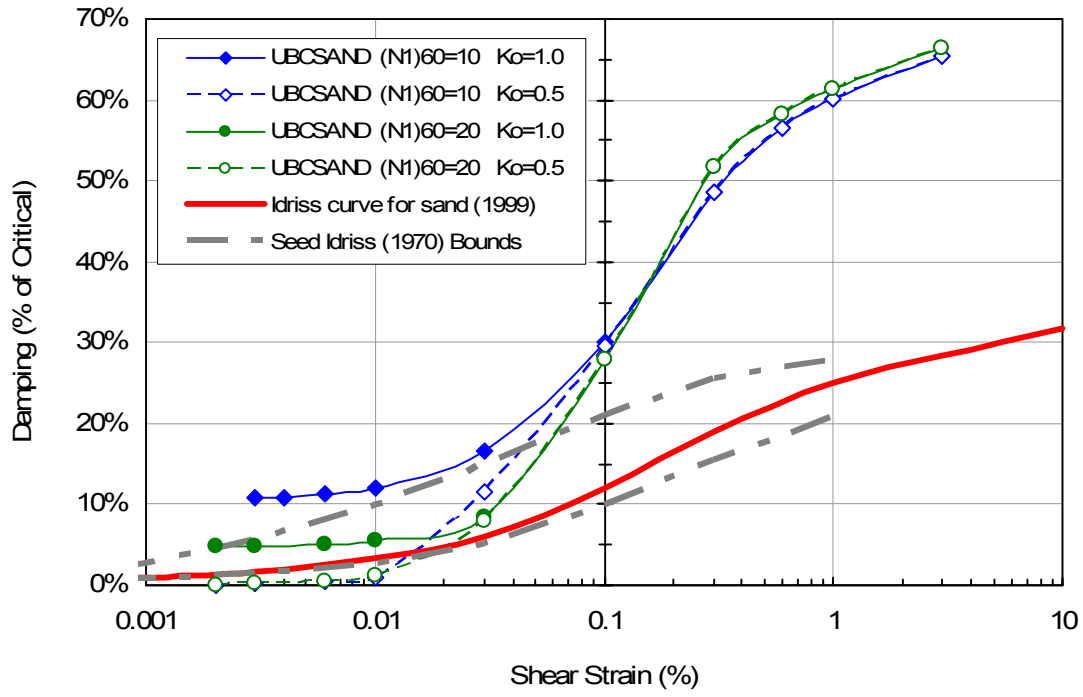

b) Damping curves.

Figure 19. Modulus reduction and damping curves estimated for UBCSAND 904aR.

4.6 Effect of confining stress

The effect of confining stress on liquefaction resistance is addressed through the K_σ factor in a simplified liquefaction evaluation. This factor modifies the cyclic resistance ratio as a function of the initial vertical effective stress. Since the natural behavior of UBCSAND may not necessarily follow a selected K_σ relationship, the desired K_σ behavior is currently approximated in UBCSAND by adjusting the plastic shear stiffness number K_{GP} to be a function of the initial effective vertical stress.

Adjustment factors m_hfac1 were developed for the 904aR version that reproduce the K_σ curve recommended by Youd et al. (2001). The exponent "f" in the K_σ equation was estimated by assuming the following relationship between relative density D_r and $(N_1)_{60}$: $D_r^2 = (N_1)_{60}/46$. The relationship between $(N_1)_{60}$, σ'_{vo}, and m_hfac1 was developed by selecting various combinations of $(N_1)_{60}$ and σ'_{vo}, applying a cyclic load equal to K_σ times the expected CRR at σ'_{vo} = 1 atm, then adjusting m_hfac1 until the cyclic DSS simulation produced liquefaction in 15 cycles. This procedure led to an equation for m_hfac1 as a function of $(N_1)_{60}$ and σ'_{vo} as described in Appendix 2. It is interesting that the estimated relationship for m_hfac1 is in the form of a power curve, similar to the adopted relationship for K_σ.

Each combination of $(N_1)_{60}$ and σ'_{vo} were evaluated at two initial values of horizontal effective stress corresponding to K_o = 0.5 and K_o = 1.0. The final calibration parameter was selected from the initial stress case that proved to be the more difficult to liquefy. In general, simulations with lower initial stresses or lower $(N_1)_{60}$ values tended to liquefy more easily at K_o = 1.0 conditions. Simulations with higher initial stresses or higher $(N_1)_{60b}$values tended to liquefy more easily at K_o = 0.5 conditions.

The resulting adjustment factors are shown in Figure 20. This figure shows m_hfac1 values greater than 1 when σ'_{vo} is less than 1 atm. Although some increase in cyclic resistance is expected at low initial confining stresses, the value of m_hfac1 would typically be limited to a maximum of the value at σ'_{vo} equal to 1 atm.

Figure 21 shows the values of K_σ that were estimated using UBCSAND and the generic input parameters from Appendix 2. These estimates are directly compared to the NCEER/NSF recommendations. The relationship developed for m_hfac1 is shown to produce a good agreement with the K_σ curves. Values of K_σ were estimated for σ'_{vo} less than 1 atm both with and without the restriction on m_hfac1. Restricting m_hfac1 to the value computed for σ'_{vo} = 1 atm did reduce the estimated values of K_σ at low σ'_{vo}, although these K_σ estimates were still somewhat above 1.0.

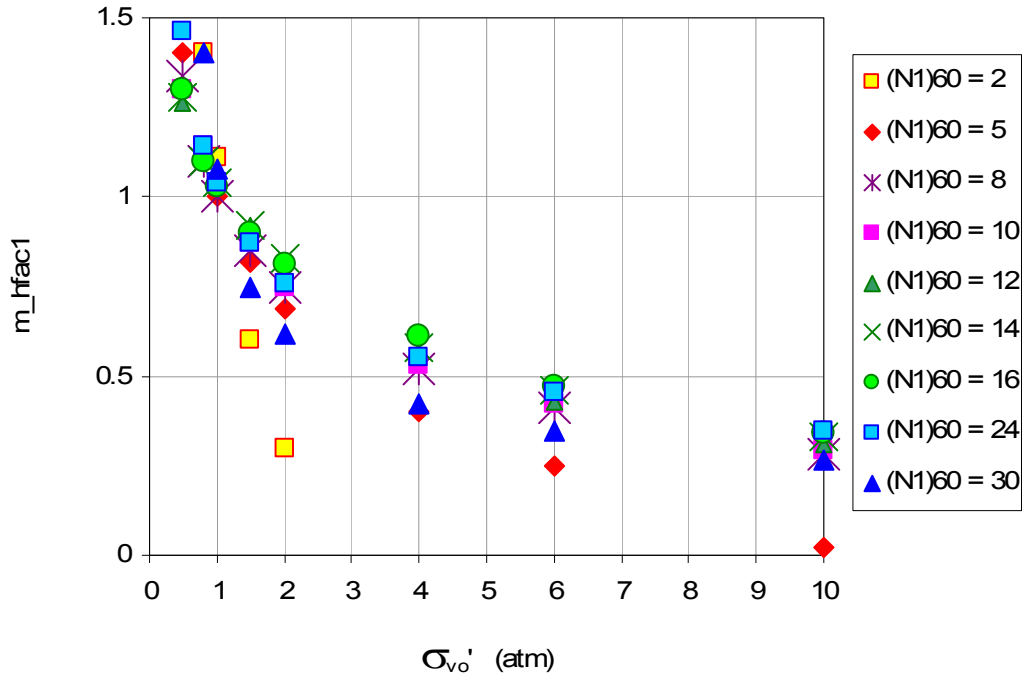

Figure 20. Calibration results showing relationship between m_hfac1, $(N_1)_{60}$, and σ'_{vo}.

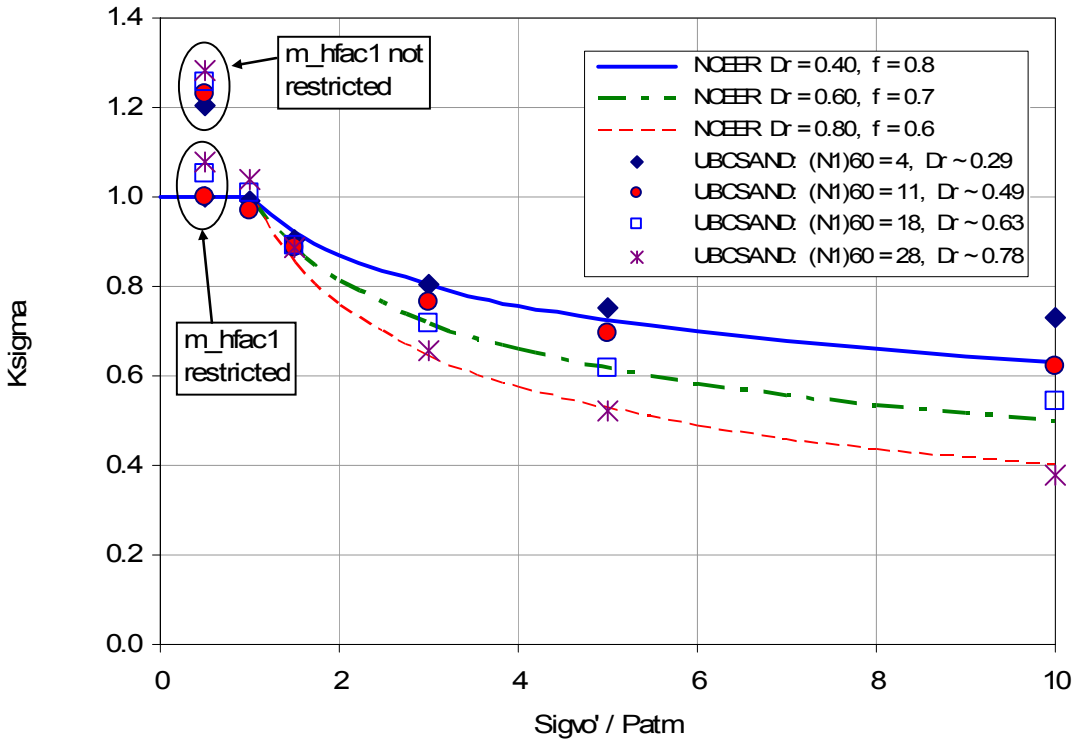

Figure 21. K_σ values estimated using UBCSAND 904aR and generic input parameters.

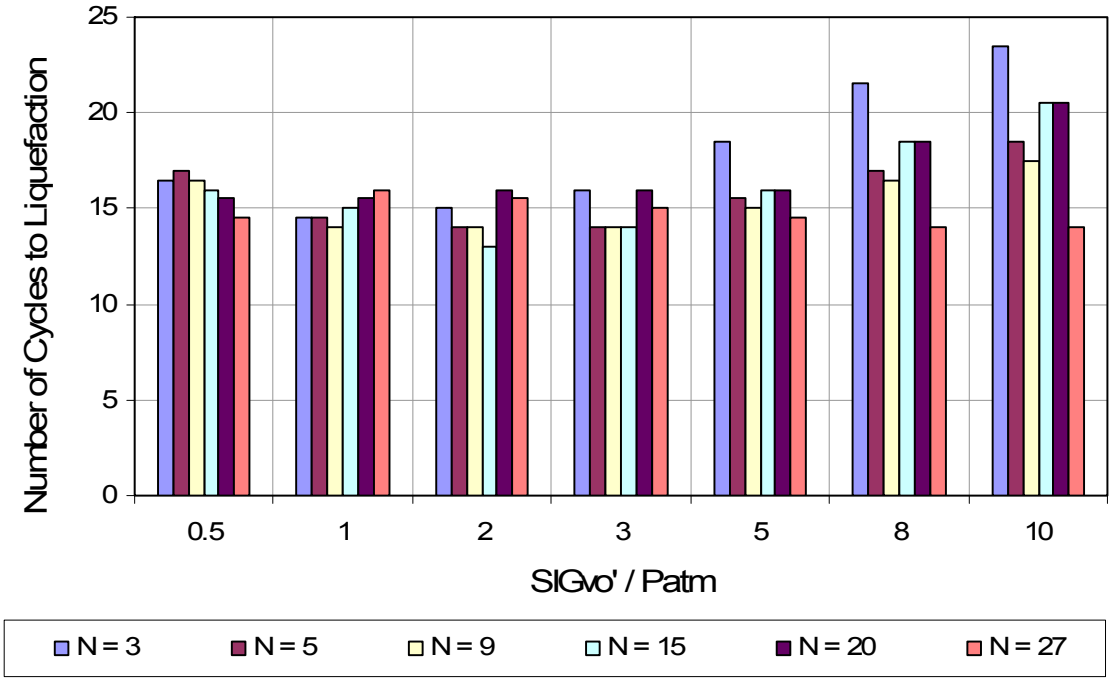

Figure 22. Predicted number of cycles to liquefaction versus σ'_{vo} and $(N_1)_{60}$ using NCEER K_σ relationship and generic equations for m_hfac1.

A similar comparison is shown on Figure 22 which relates the computed number of cycles to liquefaction versus initial effective vertical stress and blowcount. The generic input parameters were used, and the samples were loaded with a cyclic stress intended to produce liquefaction in 15 cycles at each stress level. The generic input parameters are seen to reasonably duplicate the anticipated liquefaction response, with the greatest deviation at high initial stress levels. The elements at high stress levels were somewhat more resistant to liquefaction than would be predicted from the NCEER K_σ relationship. This deviation results from approximations in the curves developed for m_hfac1.

4.7 Effect of K_o

The liquefaction response predicted by UBCSAND is a function of K_o, the ratio of the initial horizontal effective stress to the initial vertical effective stress. Some relationship is anticipated between K_o and CRR since liquefaction resistance should be influenced by the initial mean effective stress (e.g., the mean effective stress has a strong influence on the shear stiffness response, which in turn relates to the pore pressure generation). However, this relationship appears to be exaggerated in UBCSAND since the plastic effects of principal stress rotation are not considered.

The rotation of principal stress can be a problem in any constitutive model based on classical plasticity when the direction of maximum shear stress is not coincident with the direction of the applied cyclic loading. As a shear load is applied to the model and plastic strains are generated, the direction of maximum shear stress will tend to rotate until it approximates the direction of the applied shear loading. This rotation should generate plastic shear and volumetric strains, but these additional strains are not considered in the UBCSAND model.

The effect of K_o was considered during the calibration of UBCSAND. Several trends were noted when performing DSS simulations of undrained sands using UBCSAND with an applied cyclic load equal to CRR_{15}. It was observed that sands with relatively low values of $(N_1)_{60}$ tended to liquefy more easily at $K_o = 1$ than at $K_o = 0.5$. In contrast, sands with high values of $(N_1)_{60}$ tended to liquefy more easily at $K_o = 0.5$ than at $K_o = 1.0$. It was also noted that this relationship was a function of σ'_{vo}. At a low stress a sand might liquefy more easily at $K_o = 0.5$, while that same sand would liquefy more easily at $K_o = 1.0$ at a higher stress level.

To address the influence of K_o on liquefiability, UBCSAND was calibrated considering both $K_o = 0.5$ and $K_o = 1.0$. Whichever initial stress state was found to be the more difficult to liquefy was selected for use in the calibration. Once the calibrations were completed, the effect of K_o on the liquefiability of the model was investigated. A series of DSS simulations were performed for various $(N_1)_{60}$ values and for σ'_{vo} values of 1 atm and 4 atm. The applied cyclic load was CSR_{15}. A number of analyses were performed at each $(N_1)_{60}$ value by changing the initial K_o value. The number of cycles to liquefaction was then determined at each K_o value. The number of cycles would approach 15 at either $K_o = 0.5$ or $K_o = 1.0$ depending on how the calibration had been performed. At other values of K_o the required number of cycles would vary.

To help evaluate the trend of liquefiability versus K_o, the predicted number of cycles at each K_o was converted into an equivalent CRR_{15} using the weighting curves developed for UBCSAND in Section 4.3. The resulting curves reveal the direct relationship between CRR_{15} and K_o as shown in Figure 23. This relationship is seen to be fairly subtle for $K_o < 1$ and $(N_1)_{60} > 10$ - 15. Significantly reduced values of CRR_{15} (i.e., more liquefiable) can occur for smaller $(N_1)_{60}$ values with K_o near unity. All values of $(N_1)_{60}$ tended to be significantly more resistant to liquefaction at higher values of K_o.

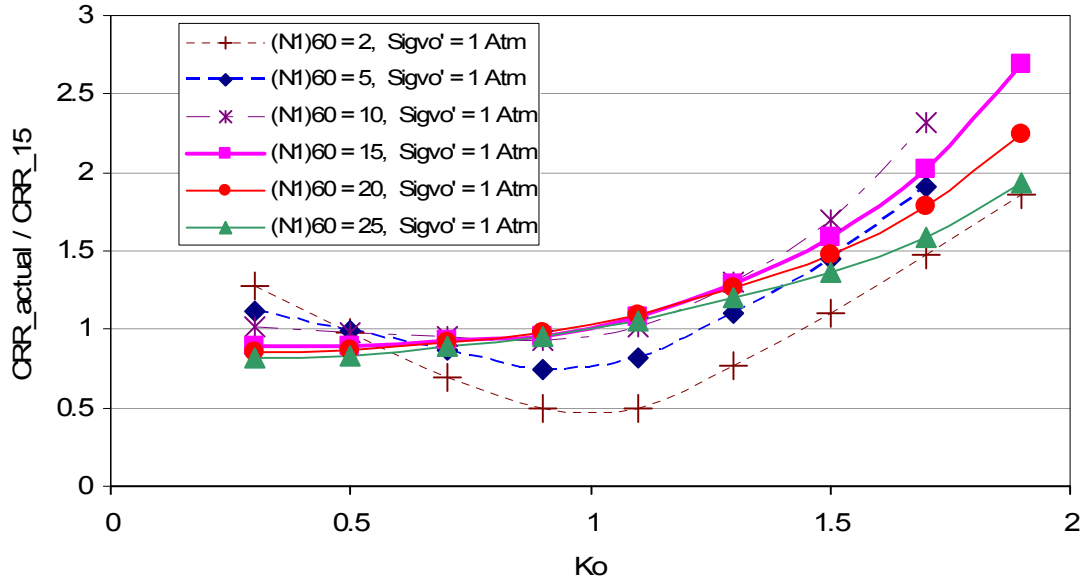

a) σ'_{vo} = 1 atm

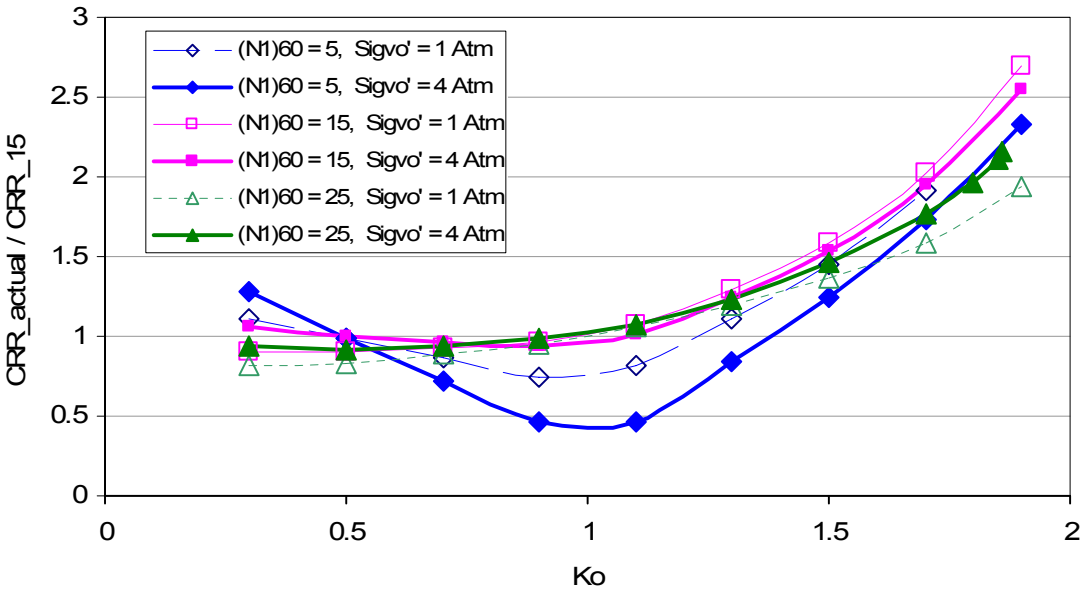

b) Comparison of σ'_{vo} = 1 atm and σ'_{vo} = 4 atm.

Figure 23. Predicted relationship between K_o and CRR_{15} for UBCSAND 904aR.

4.8 Rate of excess pore pressure generation and volumetric strain

The rate of excess pore pressure generation predicted by UBCSAND was evaluated by comparing published trends from laboratory tests with trends predicted from DSS simulations. The data from the DSS simulations used the analyses previously described in Section 4.1.

Figure 24 compares the rate of excess pore pressure generation (r_u) summarized by Seed et al. (1976) to the predictions made by UBCSAND. The two sets of plots agree well, with two exceptions. The initial rate of pore pressure generation is relatively slow for the $(N_1)_{60} = 5$ material with $K_o = 0.5$. This is related to the importance of the initial stress state on the UBCSAND prediction for the low blowcount sand. The second deviation occurs when liquefaction is approached. The Seed et al. trend shows a rather smooth increase towards a fully liquefied state, while the UBCSAND predictions become a bit irregular as the element approaches liquefaction. Some of these fluctuations are due to the cycles of dilation and contraction that are predicted near the occurrence of liquefaction. The UBCSAND predictions appear smoother and are in better agreement with the Seed trends if only the maximum r_u from each half cycle is plotted.

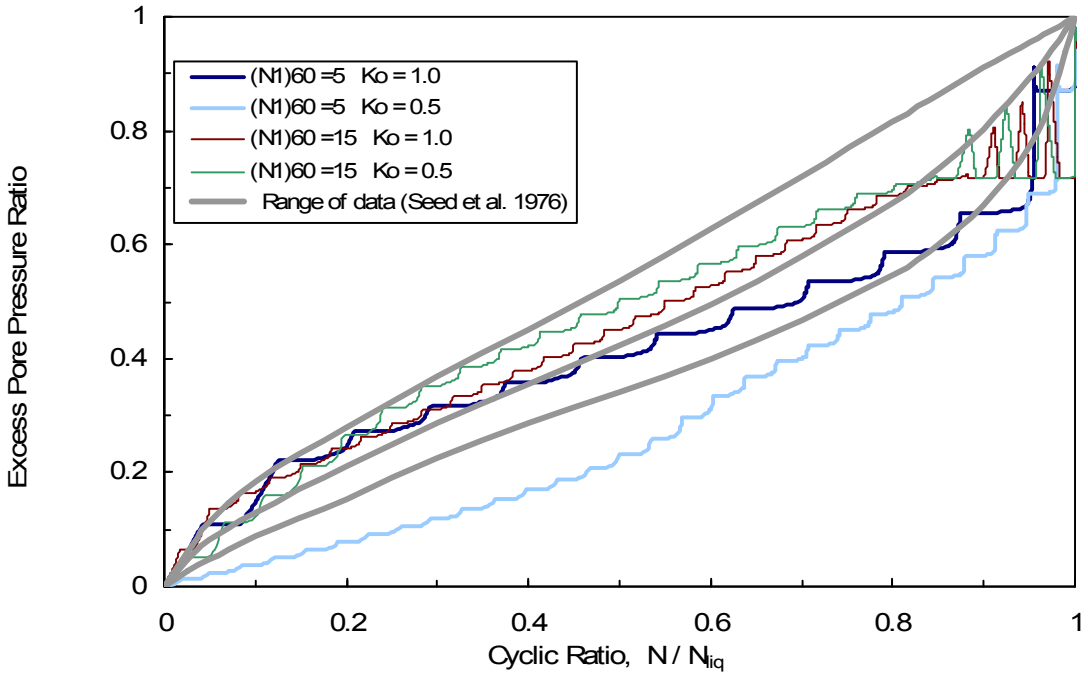

Figure 24. Rate of excess pore pressure generation from UBCSAND 904aR versus trend reported by Seed et al. (1976).

Figure 25 compares the relationship between factor of safety for liquefaction FS_{LIQ} versus r_u. The published trend used for the comparison is from Marcuson et al. (1990). FS_{LIQ} is defined as the CSR that will liquefy the element in a given number of cycles divided by the CSR that is actually applied to the element for that same number of cycles. The corresponding r_u value is the maximum value obtained during the given number of loading cycles. The same combination of $(N_1)_{60}$, K_o, and CSR were investigated as shown in Figure 24. The values of r_u versus FS_{LIQ} predicted by UBCSAND give reasonable agreement with the published trend. UBCSAND appears to predict somewhat larger increases in pore pressure due to small loading cycles than would be expected from the published information.

4.9 Comparison to cyclic DSS data on Fraser River sand

A direct comparison between the 904aR model and cyclic laboratory data in DSS is shown in Figure 26 through Figure 29. The data is from tests performed at the University of British Columbia on Fraser River sand. The sand was reconstituted by air pluviation to a relative density D_r of 40%. While the 904a version is not capable of simulating the observed increase in pore pressure for the cases that do not have a shear stress reversal, the 904aR version is seen to give a reasonable representation of the observed pore pressure response.

The input parameters for the UBCSAND analysis were developed by first noting that the sample with no static bias and an applied CSR of 0.08 had liquefied in 17 cycles. The UBCSAND model was then run under the same loading conditions using the generic input parameters. The $(N_1)_{60}$ that is used to define these parameters was then adjusted until the UBCSAND element liquefied in 17 cycles. An $(N_1)_{60}$ value of 6.9 was required to achieve liquefaction in 17 cycles, which suggests $D_r^2 \approx (N_1)_{60} / 43$ for this sand. These simulations were run with an initial K_o of 0.5.

Figure 26 shows the comparison between the laboratory data and the UBCSAND simulation for the case of no static bias. Some significant differences are noted. One difference is the rate of pore pressure generation, which initially increases at a slower rate than was observed in the laboratory. This is due, in part, to how principal stress rotation is addressed in UBCSAND: stress rotation with no change in maximum stress ratio produces an elastic response. This stress rotation component is relatively significant in the early stages of the DSS simulation. This causes the initial load increments in the simulation to generate a reduced plastic response until the internal stresses rotate and become aligned with the applied load increments. For this simulation, about 9 load cycles are required before the horizontal effective stress becomes equal to the vertical effective stress. To address this simplification in the UBCSAND model, the plastic stiffness parameters of the model have been softened during the calibration process so that the full excess pore pressure is still achieved in the correct number of cycles.

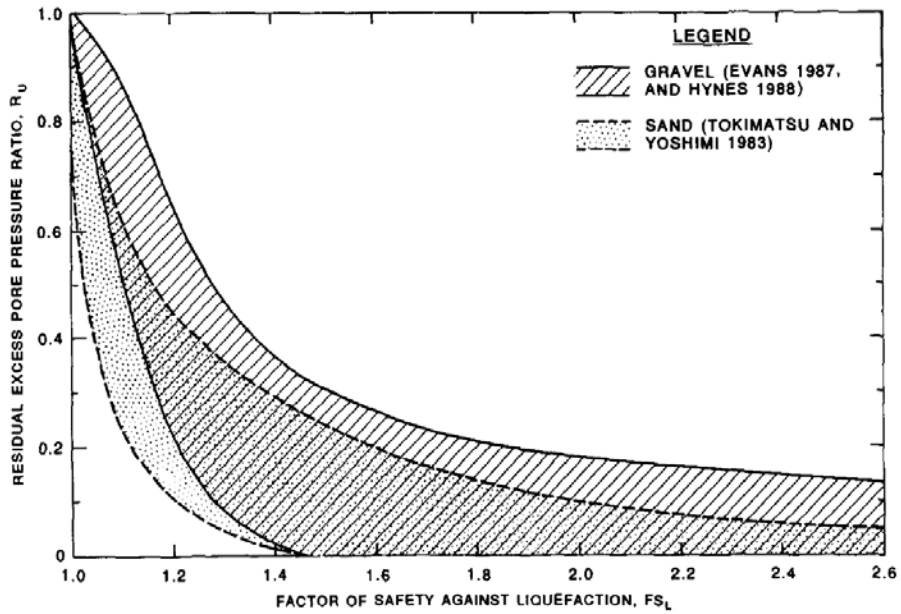

a. Typical relationships between r_u and FSLIQ from laboratory data (from Marcuson et al. 1990)

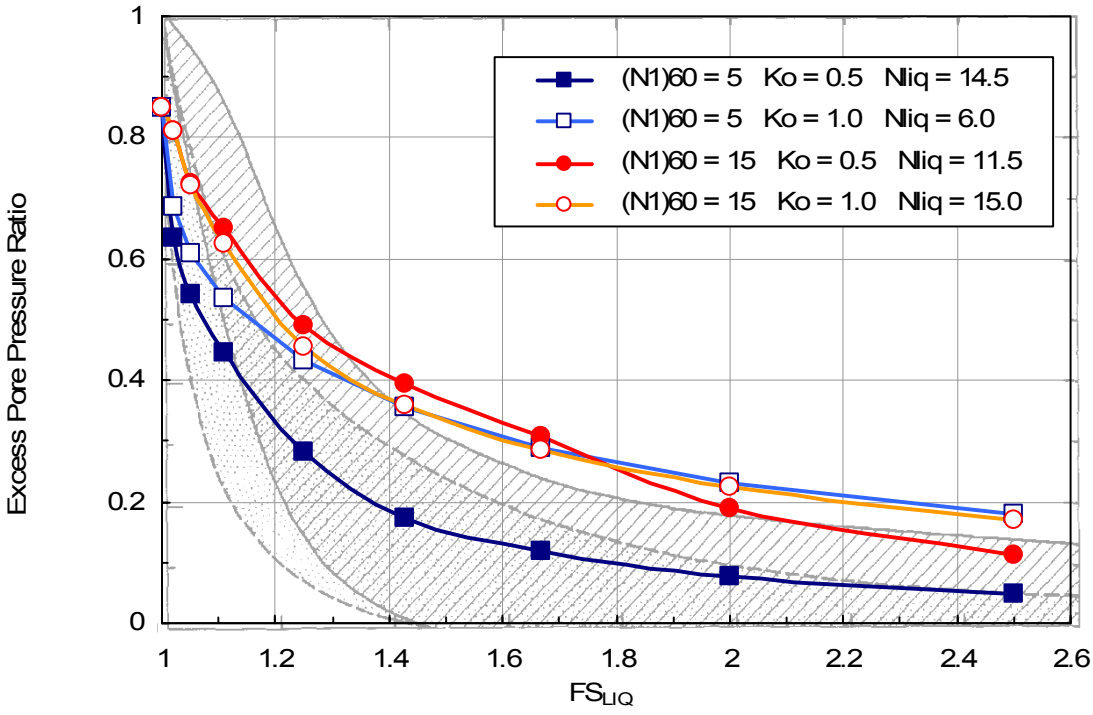

Figure 25. Rate of excess pore pressure generation from UBCSAND 904aR versus trend reported by Seed et al. (1976).

Another significant difference between the laboratory data and simulation is the stiffness of the element prior to liquefaction. The UBCSAND model predicts a stress-strain response that is approximately 5 to 7 times stiffer than observed in the laboratory. This is due to differences between the assumptions of the generic input parameters and the specific properties associated with this sand. The maximum shear stiffness estimated from the laboratory data appears to be somewhat smaller than is normally expected from sand with a relative density of 40%. For example, using the Tokimatsu and Seed (1987) relationship between G_{max} and $(N_1)_{60}$, a sand with an $(N_1)_{60}$ of 6.9 and an initial mean effective stress of about 60 kPa would be expected to have a G_{max} of about 65000 kPa. The initial load cycles measured in the laboratory and shown on Figure 26 show a cyclic strain of approximately 0.10%. The anticipated secant modulus at this strain level is expected to be about 80% of G_{max}, or about 50000 kPa. The effect of a modest increase in pore pressure will tend to reduce this modulus somewhat. But the corresponding secant modulus determined from the laboratory data is only 9000 kPa, or about 1/6 of the anticipated value. This difference between observed and predicted response could be addressed through a material-specific calibration.

To evaluate the effect of principal stress rotation on the predictions, the analysis shown in Figure 26 was repeated with an initial K_o of 1.0. Using this K_o value means the cyclic loading will be coincident with the direction of maximum shear strain at the start of loading. A new representative $(N_1)_{60}$ of 8.0 was selected to achieve liquefaction in 17 cycles. The predicted results are shown on Figure 27. The K_o = 1 simulation is shown to provide a much closer representation to the laboratory test results. The increase in pore pressure with load cycles is an almost identical match, and the plot of stress path is more similar, particularly in the earlier load cycles. There is still a discrepancy between the stiffness revealed in the stress-strain plots, although the stiffness of the K_o = 1 simulation is somewhat softer than for the K_o = 0.5 simulation.

Figure 28 provides a comparison for the same conditions and input parameters except for an initial static bias equivalent to $\alpha = 0.106$. This produces a loading state with no stress reversals on the x-y plane. As with $\alpha = 0.0$, the initial stiffness predicted by UBCSAND and the generic input parameters is much larger than was observed in the laboratory test, and the initial rate of pore pressure generation is much slower. As a result, the UBCSAND simulation requires addition load cycles before it liquefies: 4 cycles for the laboratory test and 13 for the simulation. The loading stiffness of the simulation after several post-liquefaction cycles generally agrees with that observed in the laboratory.

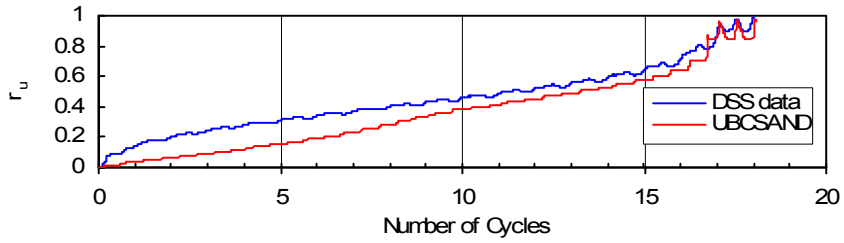

a) Rate of pore pressure generation

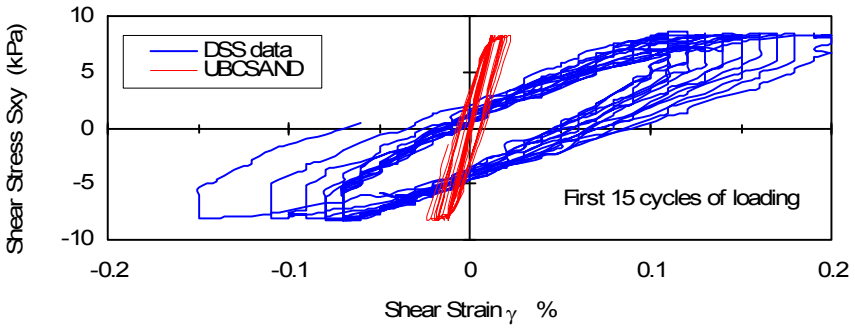

b)Stress-strain behavior (first 15 cycles)

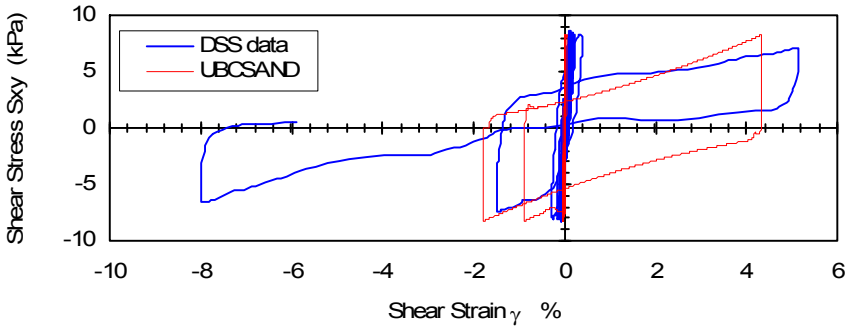

c) Stress-strain behavior

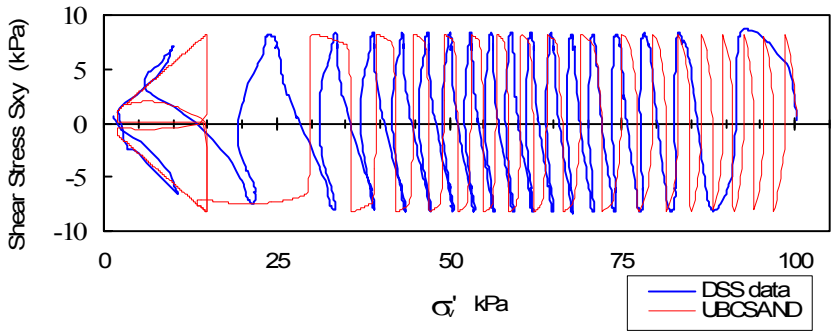

c) Stress path

Figure 26. Laboratory DSS and UBCSAND 904aR using generic input parameters (D_r = 40%, α = 0, K_o = 0.5 in simulation, and CSR = 0.0826).

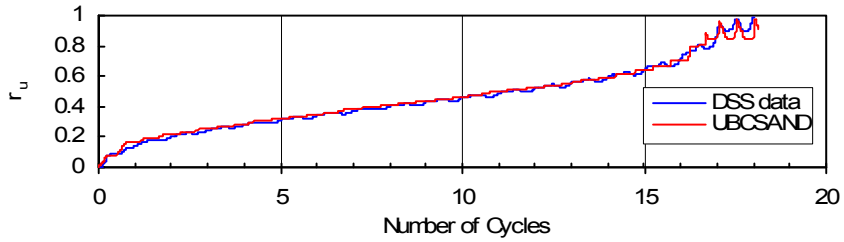

a) Rate of pore pressure generation

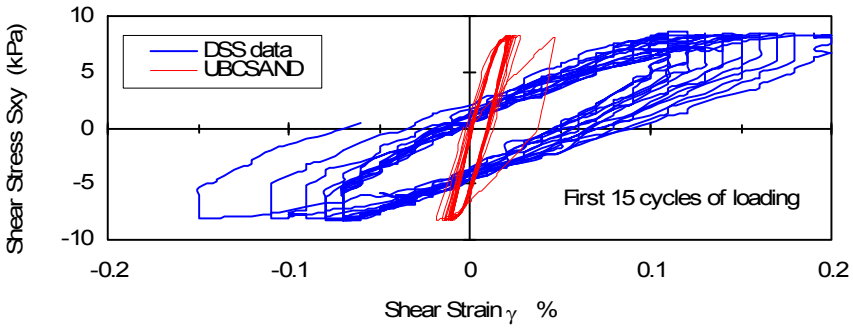

b)Stress-strain behavior (first 15 cycles)

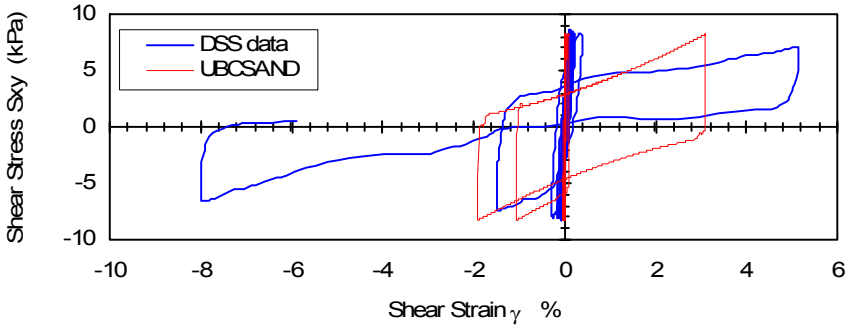

c) Stress-strain behavior

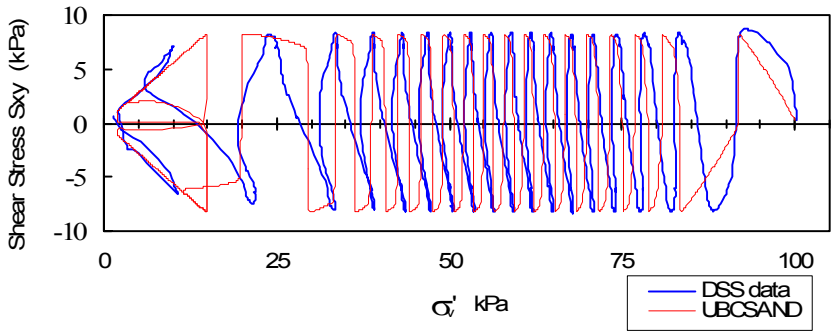

d) Stress path

Figure 27. Laboratory DSS and UBCSAND 904aR using generic input parameters (D_r = 40%, α = 0, K_o = 1.0 in simulation, and CSR = 0.0826).

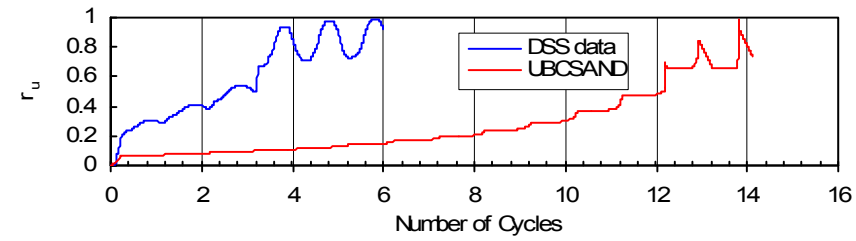

a) Rate of pore pressure generation

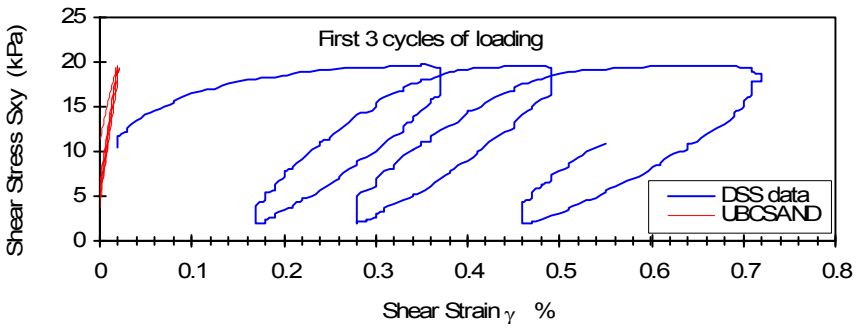

b)Stress-strain behavior (first 3 cycles)

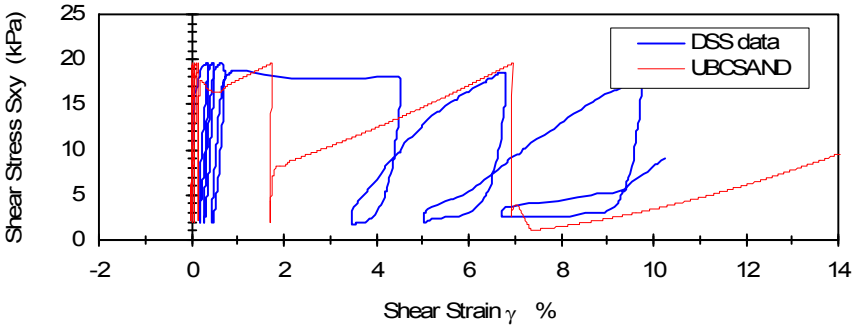

c) Stress-strain behavior

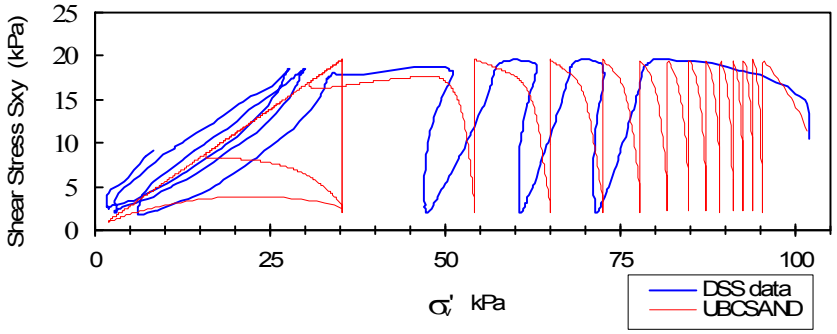

d) Stress path

Figure 28. Laboratory DSS and UBCSAND 904aR using generic input parameters (D_r = 40%, α = 0.106, K_o = 0.5 in simulation, and CSR = 0.0867).

Figure 29 compares results for the same conditions as for Figure 28 except for this case the applied CSR is only 0.06. The simulation and lab test predict a similar resistance to liquefaction: 22.5 cycles to liquefaction for UBCSAND versus 15.5 cycles for the DSS test. As with the other comparisons, the initial shear stiffness in the UBCSAND analysis is significantly stiffer than observed in the laboratory test. The other significant difference is the post-liquefaction stress strain response. The loading stiffness after liquefaction in UBCSAND is related primarily to the rate of dilation of the soil skeleton and the resulting impact on the effective stress. The post-liquefaction stiffness observed in the lab test is significantly larger than the UBCSAND prediction.

DSS tests without a static bias were performed on the same sand but at a relative density of 80%. An $(N_1)_{60}$ of 28 was used to develop the input parameters for UBCSAND using the relationship of $D_r^2 \approx (N_1)_{60} / 43$. Figure 30 shows comparisons between the DSS data and the UBCSAND simulations using the generic input properties. The applied CSR was equal to 0.29. The UBCSAND analysis again shows stiffer initial response than the laboratory data. The UBCSAND element is predicted to liquefy in 21 cycles, while the laboratory test showed liquefaction in approximately 11.5 cycles. The biggest differences between the test and simulation are seen in the stress path plot and also in the stress-strain response after liquefaction. However, the pore pressure generation and stress-strain behavior predicted by UBCSAND appear to be generally appropriate for dense sand.

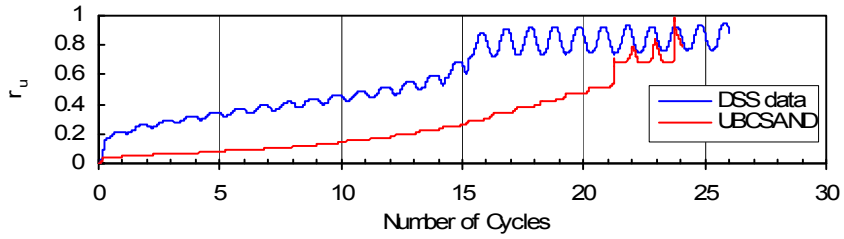

a) Rate of pore pressure generation

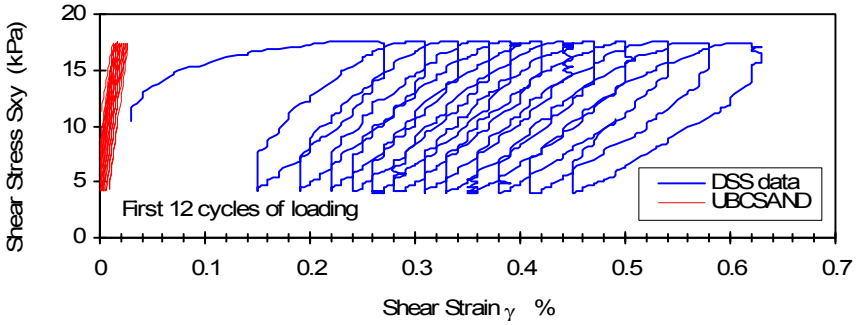

b)Stress-strain behavior (first 12 cycles)

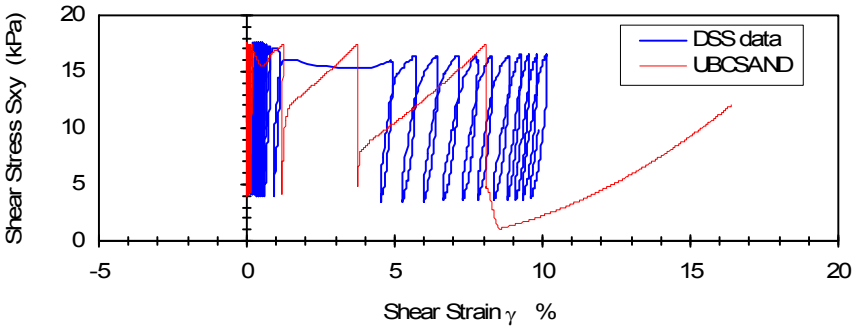

c) Stress-strain behavior

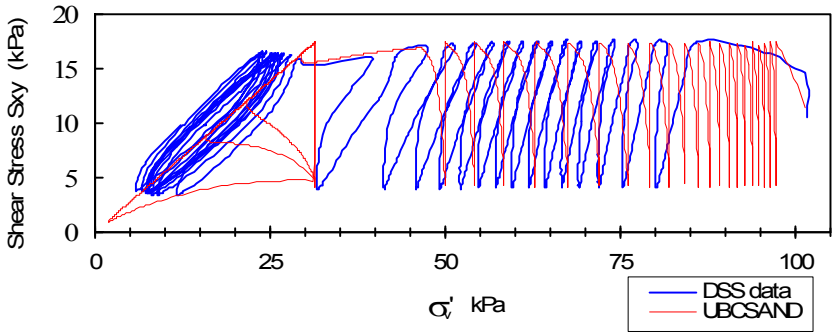

d) Stress path

Figure 29. Laboratory DSS and UBCSAND 904aR using generic input parameters (D_r = 40%, α = 0.106, K_o = 0.5 in simulation, and CSR = 0.0662).

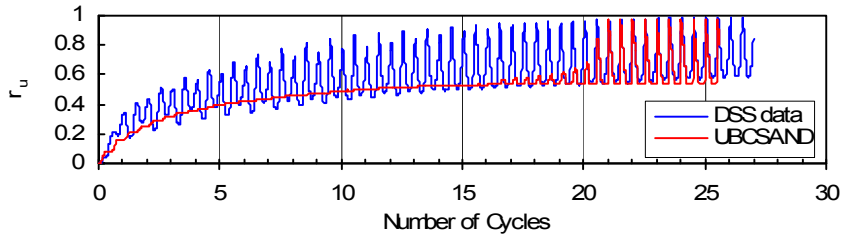

a) Rate of pore pressure generation

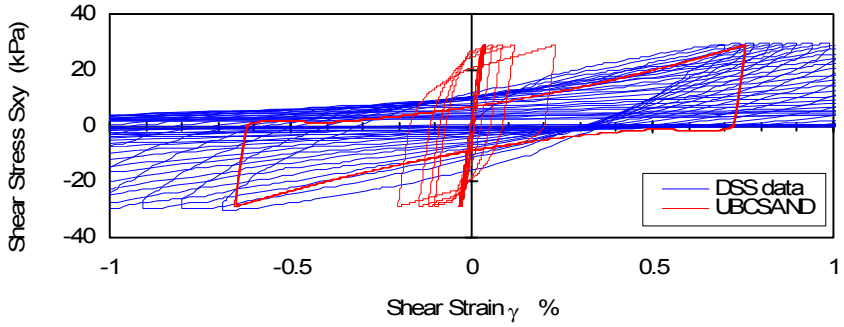

b)Stress-strain behavior (shear strains between -1% and 2% are shown)

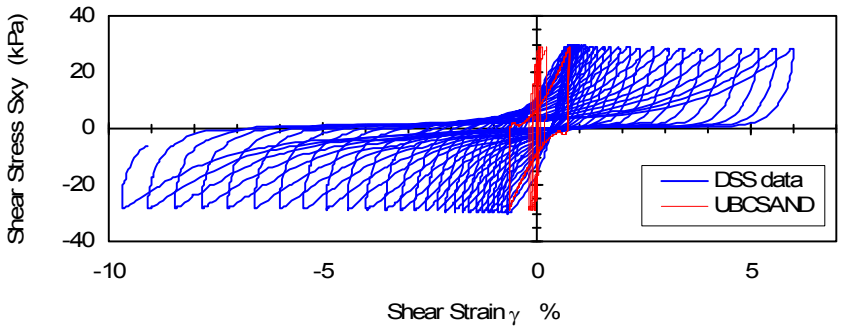

c) Stress-strain behavior

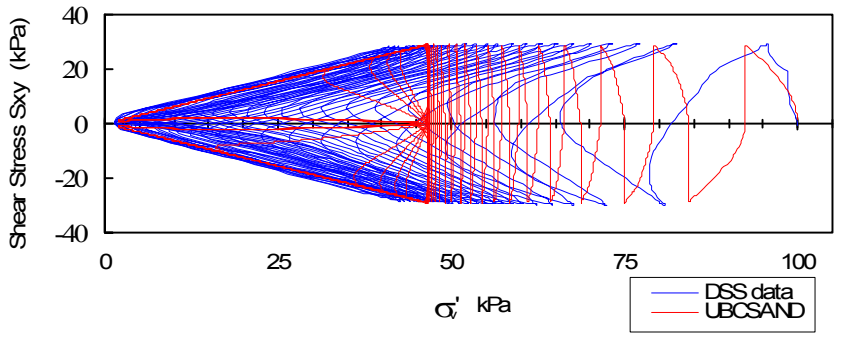

d) Stress path

Figure 30. Laboratory DSS and UBCSAND 904aR using generic input parameters (D_r = 80%, α = 0.0, K_o = 0.5 in simulation, and CSR = 0.29).

5 Post-earthquake analysis

The framework of the UBCSAND constitutive model was derived from observations made on laboratory element tests. Key aspects of the model, including the relationships between shear stiffness/effective stress/stress ratio, and between plastic volumetric strain/shear strain/stress ratio, were all derived from these general observations. Basing the model framework on high-quality laboratory tests allows a fundamental approach to the model development.

While the ability of the model to represent laboratory behavior can be demonstrated through the simulation of element tests, a critical requirement for the model is to ensure that it can simulate the behavior observed in the field. Such field behavior can be very complex due to many factors that are only approximated in the laboratory, such as complex 3-dimensional loading, pore pressure drainage, and stratigraphy on both a large and small scale.

One aspect that may not be adequately addressed by a laboratory-based model is the prediction of residual, or post-liquefaction, strengths. These strengths have been inferred from field case histories through the back analysis of observed slumps and slides (Seed and Harder, 1990; Olson and Stark, 2005). The low strength values estimated from these case histories are likely affected by complex mechanisms, such as pore water inflow, void ratio redistribution, and stratigraphic mixing. While UBCSAND will predict a significantly softened stress-strain behavior after liquefaction, the resulting mobilized strength may not be consistent with common interpretations of residual strength.

To address this concern, a post-earthquake analysis is typically run at the end of a seismic-UBCSAND analysis. This analysis is similar to a standard stability evaluation using residual strengths and limit equilibrium techniques, except both the inherent stability and the tendency for significant deformation are evaluated. This analysis is accomplished by identifying those elements that have liquefied during the earthquake. This is typically based on the maximum excess pore pressure ratio, r_u, achieved during the earthquake in each element. An r_u criterion of about 0.7 is often used. While liquefaction is often assumed to occur at r_u of 1.0, using a reduced limit reflects that zones with r_u of 0.7 may be very close to liquefaction, and that zones experiencing a sustained static bias may never reach an r_u of 1.0 despite behavior that is consistent with liquefaction. For models with low permeability barrier layers, or other problematic features, additional zones may need to be considered liquefiable based on reasonable estimates of pore water flow after the earthquake.

To implement the post-earthquake analysis, the input motion is terminated and the model is allowed to run for a period of time to allow any residual motion to decay. Zones with peak r_u values exceeding the r_u limit are then converted from the UBCSAND model to the simpler Mohr-Coulomb model. An undrained strength equal to the

residual strength is assigned and low values of shear and bulk moduli are used. For the Success Dam analyses, the shear modulus of liquefied zones was taken as 10 times the residual strength, and the bulk modulus was assigned a value equal to 100 times the shear modulus. The non-liquefied zones continue to use the UBCSAND model to permit a more accurate prediction of stress strain response due to load redistribution. The analysis is then continued in dynamic mode and the model deforms until stability is regained.

The ability of UBCSAND to dilate significantly with strain allows large strengths to be mobilized in these elements, strengths that are significantly higher than would typically be used in a post-liquefaction stability evaluation. Although these strengths could develop in the field, it is likely they would degrade as pore water flowed into the dilating zones from adjacent areas. To address this concern, the ability for UBCSAND to mobilize strength through dilation after the earthquake was limited to a maximum of the drained strength determined in each element at the start of the earthquake.

5.1 Revised r_u computation

The excess pore pressure ratio r_u in any element has traditionally been defined as $r_u = (u - u_o)/\sigma'_{vo}$, where u is the pore pressure at the time r_u is defined, u_o is the initial pore pressure, and σ'_{vo} is the initial vertical effective stress. This definition for r_u was developed for simple 1-D situations with horizontal motion such as represented by a SHAKE analysis column. In these situations, the vertical total stress does not change during to the earthquake. r_u equals zero at the start of the earthquake, and will equal 1 at the instant the effective stresses become zero. The purpose of the r_u parameter is to give a normalized measure of the pore pressure increase, with 0 indicating no increase and 1 indicating a state of liquefaction.

The traditional definition for r_u is somewhat problematic in a general 2D analysis. Total stresses change during the earthquake due to temporary fluctuations as well as permanent changes due to stress redistribution. The traditional definition for r_u can show large fluctuations during the earthquake that are not related to liquefaction. Because of permanent changes in total stress, the peak value of r_u corresponding to a liquefied element might be very different than 1, often within a range of perhaps 0.7 to 1.5.

A small change can be made to the traditional definition of r_u that maintains the original intent of this index. The excess pore pressure ratio can be defined as $r_u = 1 - \sigma'_v/\sigma'_{vo}$, where σ'_v is the vertical effective stress at the time that r_u is defined. This definition maintains much of the character of the traditional definition although it still suffers from fluctuations in r_u related to normal stress changes. However, the new r_u now equals 0 at the start of loading and 1 at the instant the effective stresses vanish. The improved stability in estimating r_u values near 1 is needed when r_u is used as a criterion for defining liquefied zones.

6 Case History Comparison

The ability of the modified UBCSAND model to predict the behavior observed in case histories was evaluated by analyzing the Upper and Lower San Fernando dams and predicting their response to the 1971 San Fernando earthquake. The cross section geometry and earthquake loading modeled for these case histories follows the original interpretation of Seed at al. (1973). The UBCSAND parameters were defined using the generic input parameters. The use of both median and 33rd percentile blowcounts was investigated.

6.1 Upper San Fernando Dam

The Upper San Fernando dam is located in southern California approximately 30 km north of downtown Los Angeles. The dam was built between 1921 and 1922 and is founded on about 15 to 18 m of alluvium overlying bedrock. The bedrock at this site is a poorly cemented conglomeritic or coarse-grained sandstone. The dam is approximately 21 m high with slopes of 2.5H:1V and incorporates a wide downstream bench. The embankment material is believed to have been hauled from the borrow area in wagons, dumped into a pond between containment dikes, and dispersed by hydraulic jetting (Seed et al. 1973). This method yielded a central clayey zone with highly stratified shells consisting of sand, silty sand, and clay. The sandy layers have a representative fines content of about 25% (Harder et al. 1989). A representative cross section as developed by Seed et al. (1973) is shown on Figure 31.

Observed seismic response

The magnitude 6.6 San Fernando earthquake occurred on February 9, 1971. The dam was located near the western edge of the observed fault rupture. Indications of possible surface rupture were observed within the reservoir of the Lower San Fernando dam a

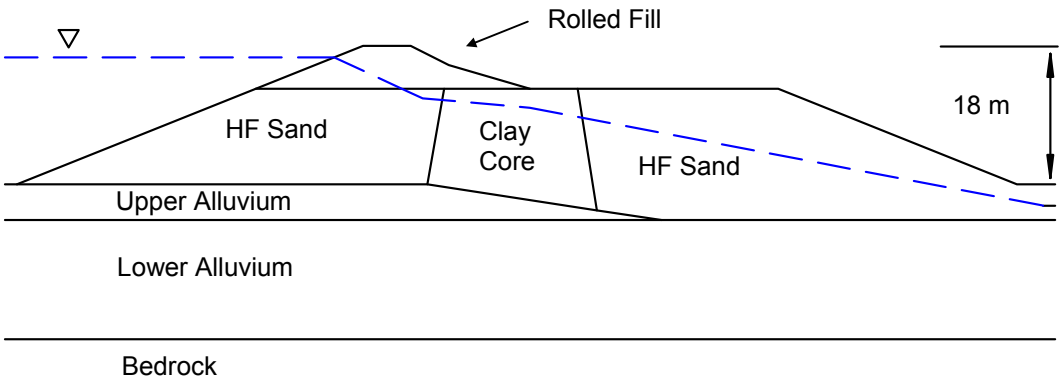

Figure 31. Representative cross-section of Upper San Fernando dam.

short distance below the dam. Peak ground accelerations (PGA) at the site were estimated to be about 0.55 to 0.6 g (Seed et al. 1973). This compares well with the median PGA estimated from several current attenuation relationships (SSA 1997).

Deformations of the dam due to the earthquake were characterized by a general downstream displacement. The crest moved horizontally in a downstream direction up to 1.5 m and dropped vertically up to 1.0 m (Harder et al. 1989). Horizontal movements of up to 2.2 m were noted on the bench at the downstream face (Serff et al. 1976). Several longitudinal cracks with offsets were also observed running the length of the upstream face near the reservoir surface.

The occurrence of liquefaction was suggested by increased water levels in the three standpipe piezometers within the embankment. Water overflowed from two of these instruments. A sinkhole was also observed in the downstream shell above a crack in the outlet conduit.

Seismic loading

The input motion selected for this analysis was the Pacoima dam record as modified by Seed et al. (1973) and shown on Figure 32. Although the input motion appears reasonable for a near field record, the actual seismic loading experienced by the dam is not known. This is a common concern in back analysis since seemingly minor differences in the character of the input motion may produce a pronounced effect on the displacement response.

The input seismic motion was converted to an equivalent shear stress history and then applied to a compliant boundary at the base. A compliant boundary was used to reduce unintended reflections off of the base of the model. The resulting motion at the base is similar to the "within" motion that would be estimated in a SHAKE analysis, although the FLAC motion also incorporates the two-dimensional influence of the overlying foundation and embankment.

The orientation of the input stress history (i.e., positive or negative polarity) was selected so that the direction of the large velocity pulse in the model was reasonably consistent with the orientation of the pulse at the Pacoima Dam recording site. Maintaining a similar orientation was considered potentially important due to the pronounced near field character of the time history.

$(N_1)_{60}$ characterization

Representative $(N_1)_{60}$ blowcounts for the hydraulic fill shells are given in Table 2. The values are based on SPT tests performed during April and May 1971 and have been corrected for confining stress, energy ratio, and the estimated densification caused by the earthquake. Both 33rd percentile and median values are provided and are

designated $(N_1)_{60\text{-}33}$ and $(N_1)_{60\text{-}50}$, respectively. The $(N_1)_{60\text{-}33}$ is intended to give a measure of the looser fraction of the soil unit.

The $(N_1)_{60\text{-}50}$ values in Table 1 have been modified from those published by Harder and others (Harder et al. 1989, Seed and Harder 1990). The correction used for earthquake-induced volumetric strain was revised to reflect the kinematic deformations predicted in finite difference analyses (Beaty 2001). In other words, the revised corrections were based on smaller estimates of volumetric strain since a portion of the observed settlements were attributed to the movement of the soil mass rather than densification. In addition, the distribution of blowcounts within the lowest hydraulic fill zone beneath the downstream shell and the zone described as Upper Alluvium beneath the upstream shell are similar. Since there were relatively few data points within each of these zones, and much of the Upper Alluvium zone was tentatively logged as hydraulic fill during the drilling, their blowcounts were combined to produce an average distribution at the base of the embankment.

Static analysis

The static analysis was performed in FLAC using a hyperbolic stress-strain model based

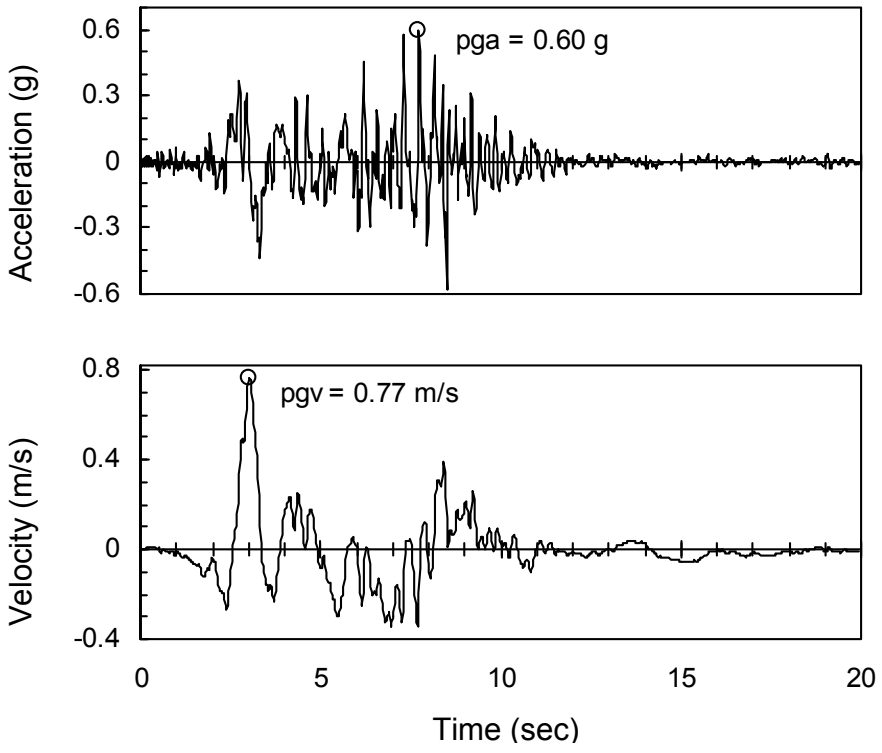

Figure 32. Modified Pacoima Dam motion from 1971 San Fernando earthquake.

Table 1. Clean sand corrected blowcounts of hydraulic fill.

Zone	Depth below crest (m)	$(N_1)_{60\text{-}50}$	$(N_1)_{60\text{-}33}$
HF (upper)	7.0 – 14.6	10	7
HF (mid)	14.6 – 18.6	14.5	11
HF (lower)	18.6 – 22.2	13	9

on the Duncan formulation (Duncan and Chang 1970). The construction and loading sequence was approximately modeled by building the embankment model in layers and then raising the reservoir in stages. The seepage calculations were performed using the groundwater flow capabilities of FLAC. This process gave a reasonable if simplified estimate of initial effective stresses and seepage forces. The material properties used in the static analysis, including stiffness, density, and strength, were based primarily on the testing and data evaluation performed during the 1973 study (Seed et al., 1973). The permeability values were approximated from the Atterberg limits and gradations using various empirical relationships, including adaptations of the Kozeny-Carman equation (Carrier, 2003; Aubertin et al., 2005). The selected values are shown on Table 2.

Seismic analysis

The seismic analysis, including liquefaction response and deformations, was performed in FLAC using various constitutive models. The revised UBCSAND model was used for the liquefiable hydraulic fill shell zones. A hysteretic model developed primarily at UBC was used for the lower alluvium, clayey core, and rolled fill zones. And a linear elastic model was assigned to the underlying rock. Zones defining the rock at the base of the model are required as part of the compliant base definition in FLAC.

The hysteretic model was developed by assuming hyperbolic shear stress-strain behavior on the horizontal plane. This model incorporates both modulus reduction and hysteretic damping in a reasonable way. Comparison of the model behavior predicted from a simple shear simulation with typical curves for modulus reduction and damping are shown in Figure 33 and Figure 34. The abrupt decrease in modulus and increase at damping that occurs between shear strains of about 0.03% and 0.1% is the result of plastic flow occurring at the yield strength of the element. In addition to the hysteretic damping, a nominal amount of Rayleigh viscous damping equal to 0.5% of critical was assigned using a center frequency of 1.0 Hz.

Table 2. Properties used for static analysis, USFD.

Property	Units	Hyd. Fill	Clay Core	Rolled Fill	Lower Alluvium	Rock
γ_{sat}	pcf	122	122	140	129	140
γ_{mst}	pcf	120	120	134	120	140
cohesion	psf	0	0	100	0	—
ϕ	º	37	37	37	37	—
K_{ge} [1]	—	420	420	300	280	—
n_e [1]	—	0.52	0.52	0.76	0.8	—
R_f [1]	—	0.78	0.78	0.9	0.66	—
K_b [2]	—	233	233	166.7	155	—
m_e [2]	—	0.52	0.52	0.76	0.8	—
porosity	—	0.5	0.5	0.5	0.5	0.5
kxx	cm/s	1e-3	1e-5	1e-5	5e-2	—
kyy	cm/s	1e-4	1e-5	1e-5	5e-3	—
G	psf	—	—	—	—	4.7e7
B	psf	—	—	—	—	6.3e7

1 Defines hyperbolic relationship for shear stress versus strain:

$$G_{\tan gent} = K_{ge} \times P_{atm} \times \left(\frac{\sigma'_m}{P_{atm}} \right)^{n_e} \times \left(1 - R_f \times \frac{\tau}{\tau_{failure}} \right)^2$$

2 Defines relationship between elastic bulk modulus and mean confining stress:

$$B = K_b \times P_{atm} \times \left(\frac{\sigma'_m}{P_{atm}} \right)^{m_e}$$

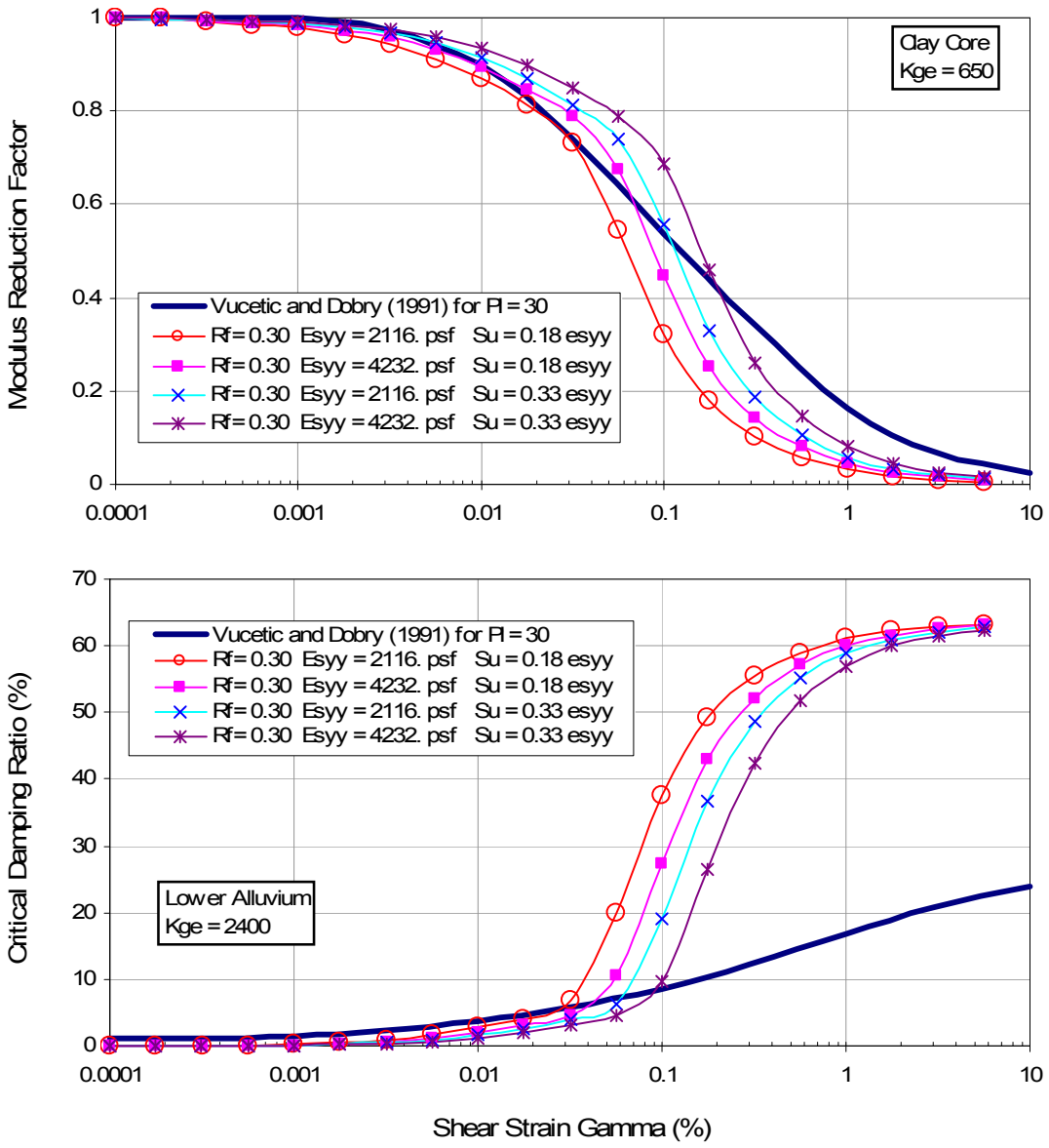

Figure 33. Modulus reduction and damping behavior of hysteretic model in simple shear using parameters for clay core.

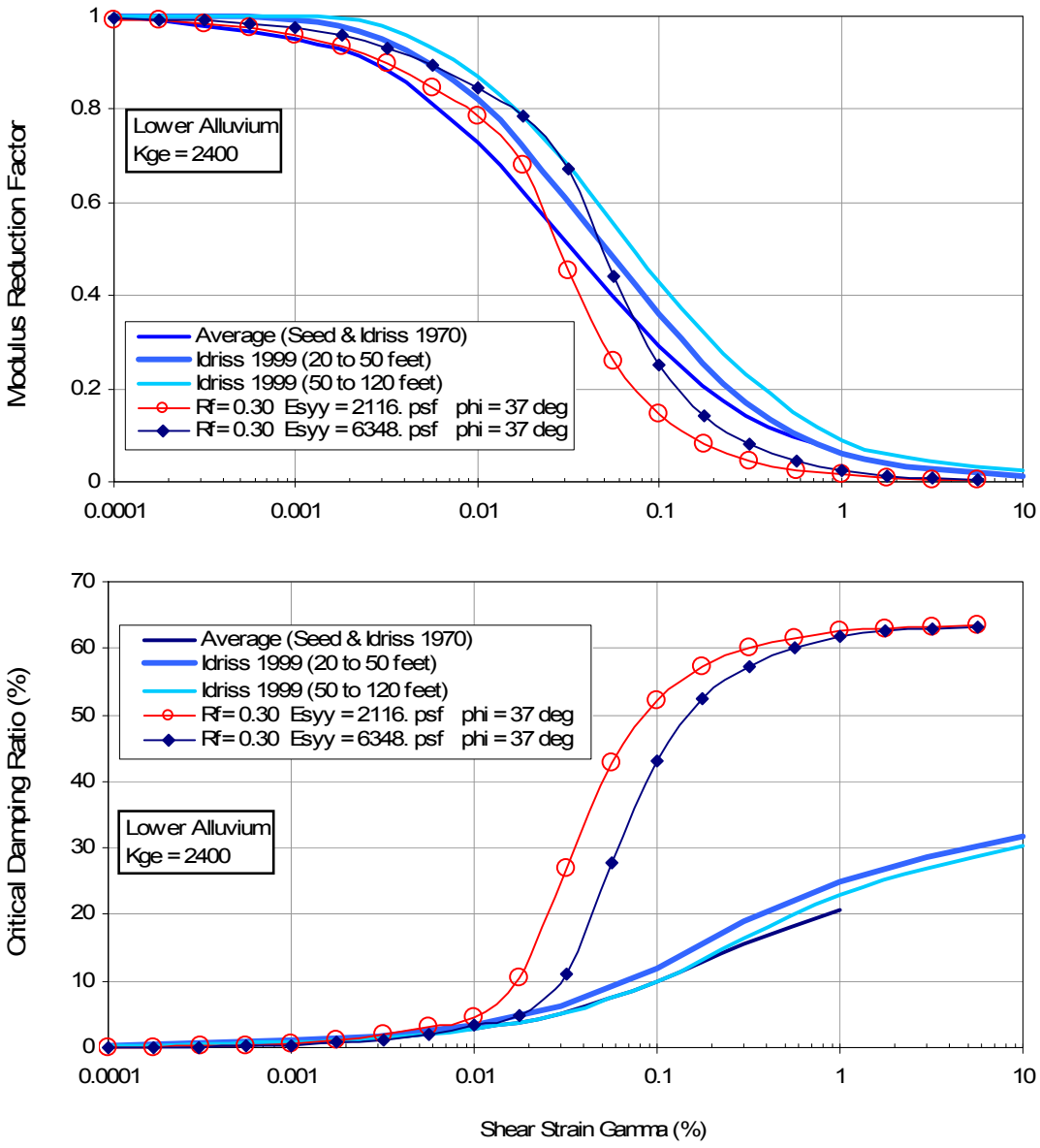

Figure 34. Modulus reduction and damping behavior of hysteretic model in simple shear using parameters for lower alluvium.

The additional properties used to define the seismic analysis are shown in Table 3. The range in undrained strength values for the clayey core is approximate. The range was estimated from torvane test results (Seed et al., 1973) as well as limited CPT tests reported by Bardet (1995). The generic UBCSAND properties were used in conjunction with blowcounts corrected to clean sand conditions. The primary analyses assumed properties based on $(N_1)_{60\text{-}50}$ (or median) blowcounts The Idriss and Boulanger (2006) correction for fines content was used, which added 5 blows to each blowcount for an average fines content of 25%. The Idriss and Boulanger (2007) curve for residual strength S_r was used as shown in Figure 35. The fines content correction for $(N_1)_{60}$ and S_r was 2 blows for an average fines content of 25%. The residual strength was limited to the drained strength in any element.

Table 3. Properties used for seismic analysis, USFD.

Property	Units	Hyd. Fill	Clay Core	Rolled Fill	Lower Alluvium	Rock
S_u/σ'_{vo}						
Case 1	—	—	0.13	—	—	—
Case 2	—	—	0.25 / 0.13 [3]	—	—	—
S_u	psf	—	—	$100*\cos(37) + \sigma'_{mo}*\sin(37)$	$\sigma'_{mo}*\sin(37)$	—
K_{2max}	—	—	30	52	110	—
V_s	—	—	—	—	—	3300
K_{ge} [1]	—	—	650	2400	1150	—
n_e [1]	—	—	0.5	0.5	0.5	—
R_f [1]	—	—	0.3	0.3	0.3	—
K_b [2]	—	—	650	2400	1150	—
m_e [2]	—	—	0.5	0.5	0.5	—
G	psf	—	—	—	—	4.7e7
B	psf	—	—	—	—	6.3e7

1 Defines hyperbolic relationship for shear stress versus strain.

2 Defines relationship between elastic bulk modulus and mean confining stress.

3 Peak strength ratio = 0.25. Once peak strength is reached in an element, available strength ratio reduces to 0.13 in that element.

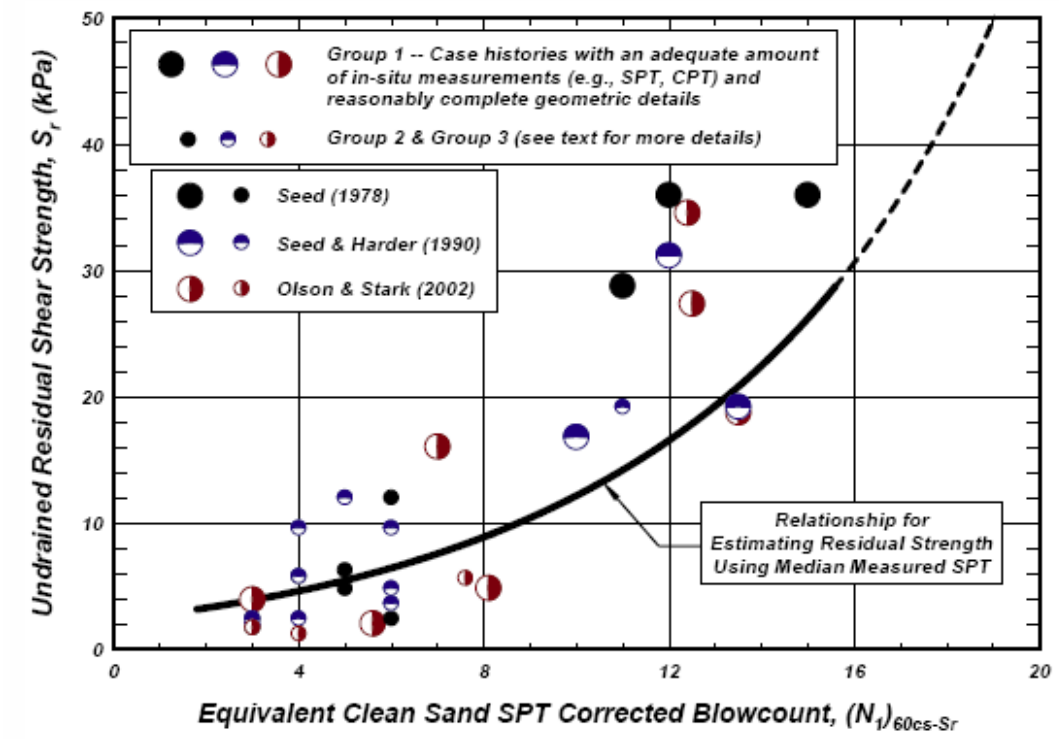

$$S_r = exp\left(\frac{(N_1)_{60cs-Sr}}{5.1} - \left(\frac{(N_1)_{60cs-Sr}}{16.5}\right)^2 + \left(\frac{(N_1)_{60cs-Sr}}{21.4}\right)^3 + 0.8\right)$$

Figure 35. Residual strength curve (copied from Idriss and Boulanger (2007)).

A limited number of parametric studies were performed. Parameters investigated include various assumptions for undrained core strength as described in Table 3, the effect of using $(N_1)_{60\text{-}33}$ blowcounts on triggering in the hydraulic fill, the difference in response between 904a and 904aR, and the use of alternative values of hydraulic conductivity in the hydraulic fill shells.

Base analysis predictions

The base analysis uses median blowcounts and a strength ratio of 0.13 in the clayey core. The stress state just before the start of earthquake loading is shown in Figure 36 while the initial pore pressure distribution is presented on Figure 37. This figure also shows the ground water levels measured in three observation wells shortly before the earthquake. These simple measurements suggest the FLAC seepage analysis predicts a

reasonable if somewhat low estimate of pore pressure within the downstream shell of the embankment.

Results from the base dynamic analyses are presented in Figure 38 to Figure 41. These figures provide the final response predictions at the end of the post-earthquake analysis.

Figure 38 shows the extensive areas of high excess pore pressure that have been predicted within the upstream shell and near the base of the downstream shell. Much of the saturated hydraulic fill in the upstream shell is predicted to liquefy, except for a fairly substantial zone near the core.

Figure 39 shows contours of maximum shear strain predicted within the dam. The highest shear strains occur near the base of the downstream shell and are associated with a pronounced downstream movement. Shear strains within the upstream shell are smaller in magnitude and somewhat more dispersed. The strains in the upstream shell indicate a shallow circular slip as well as a more deep-seated movement along the base of the shell.

Figure 40 presents the final estimate of displacement vectors. The vectors show predominantly downstream movement of the dam, which generally agrees with the actual observations and measurements of dam response. A pronounced movement of the upstream shell into the reservoir is also predicted. However, limited observations made after the earthquake do not suggest such large movements of the upstream shell. The crest is predicted to settle almost vertically with little net lateral movement, while actual measurements show the crest moving significantly downstream.

The differences between observed and predicted displacement are most clearly seen on Figure 41. In general, the magnitude and orientation of the predicted displacement are in reasonable agreement with the observed response. The 904aR analysis appears to overpredict movements of the upstream shell into the reservoir, which affects both the lateral and vertical movements predicted at the crest. Movements along the top of the downstream berm appear to be well predicted by the 904aR analysis, although it should be noted that the analysis does not include settlements due to post-earthquake consolidation. Displacements along the downstream slope of the dam are significantly overpredicted by the model. The actual displacement measurements, although limited, suggest that strains within the downstream shell were more uniformly distributed over the height of the fill. This conclusion was developed during the initial 1973 study (Seed et al. 1973). In contrast, the strains predicted in the 904aR analysis tend to be concentrated near the base of the hydraulic fill.

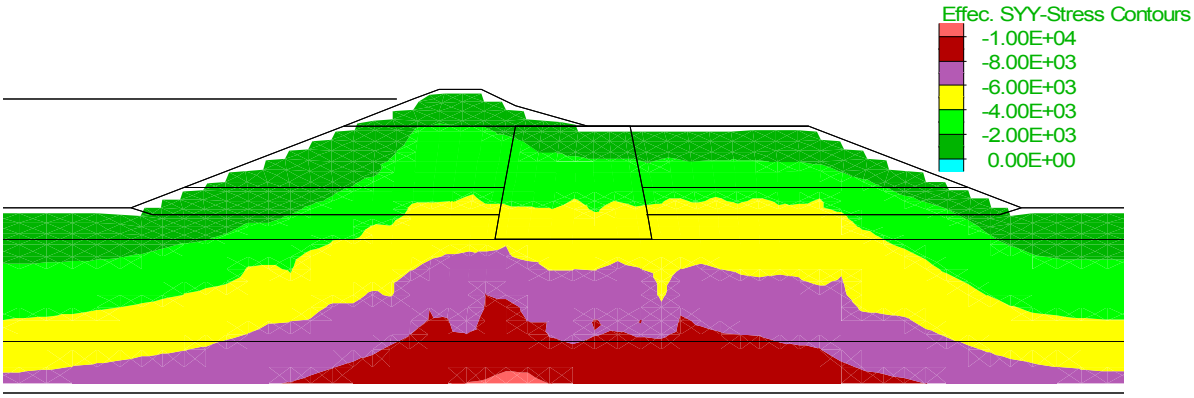

a. Effective vertical stress (psf)

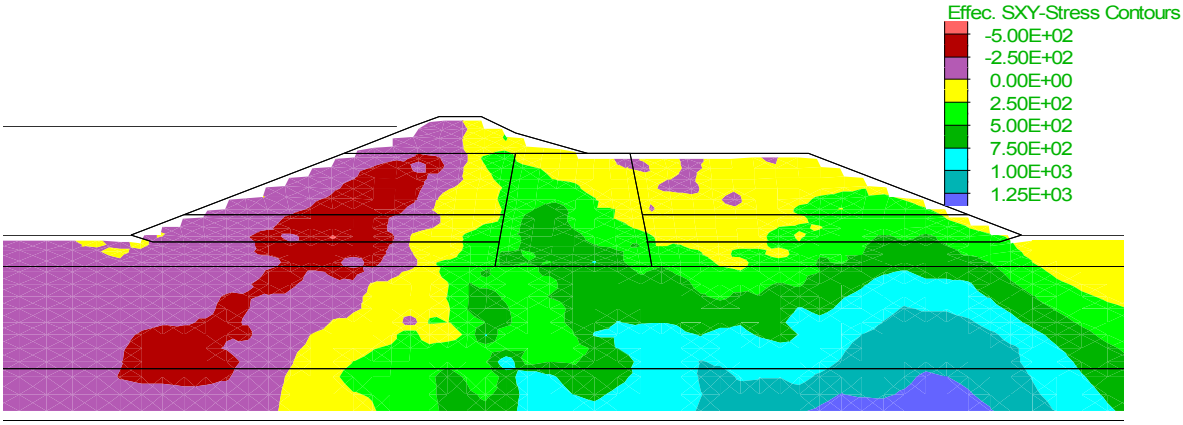

b. Shear stress τ_{xy} (psf)

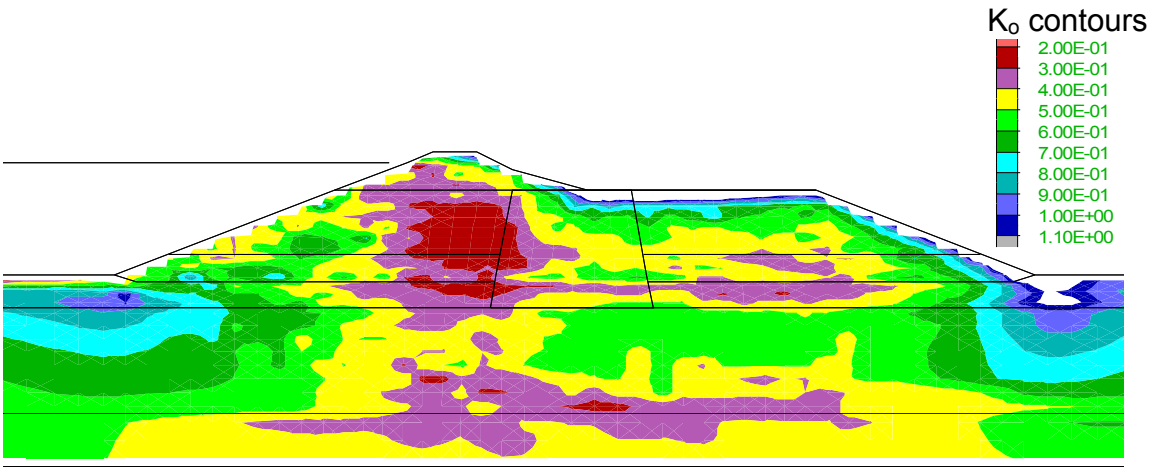

c. K_o contours

Figure 36. Predicted stress state at start of earthquake (base analysis).

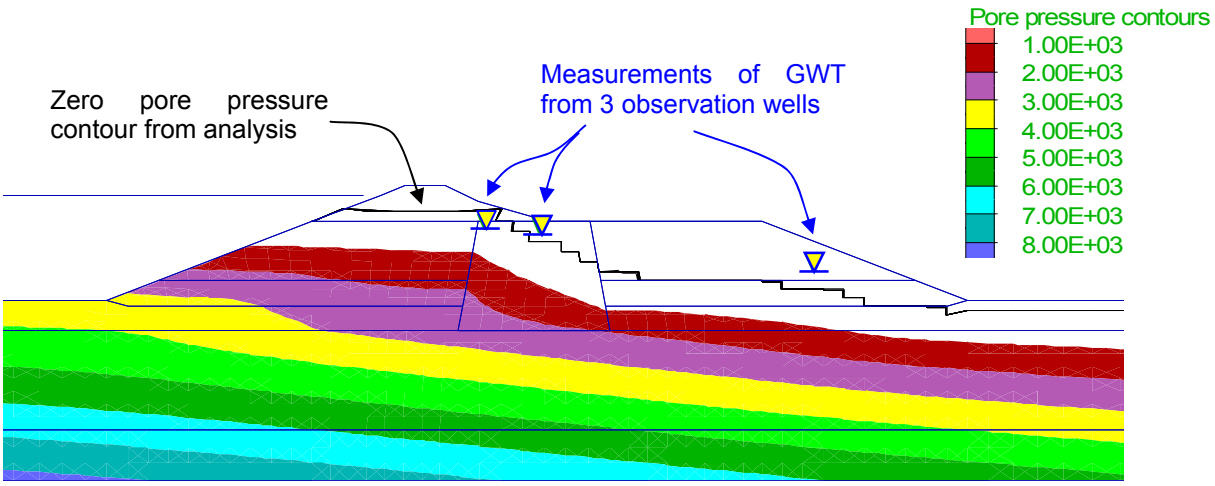

Figure 37. Predicted pore pressures at start of earthquake (base analysis).

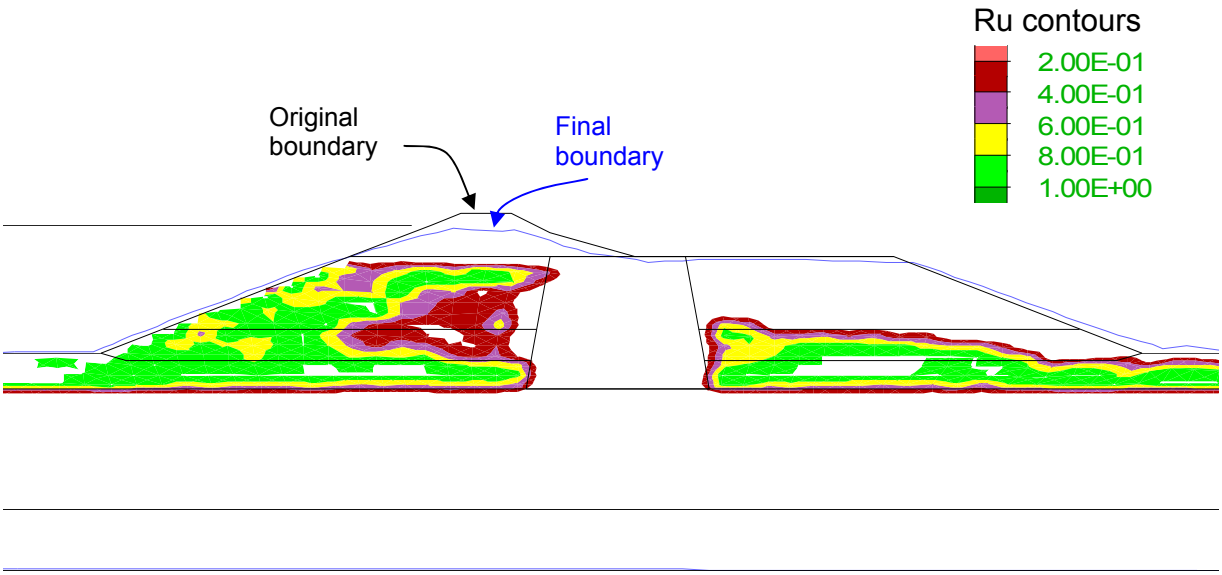

Figure 38. Peak estimates of pore pressure ratio (base analysis).

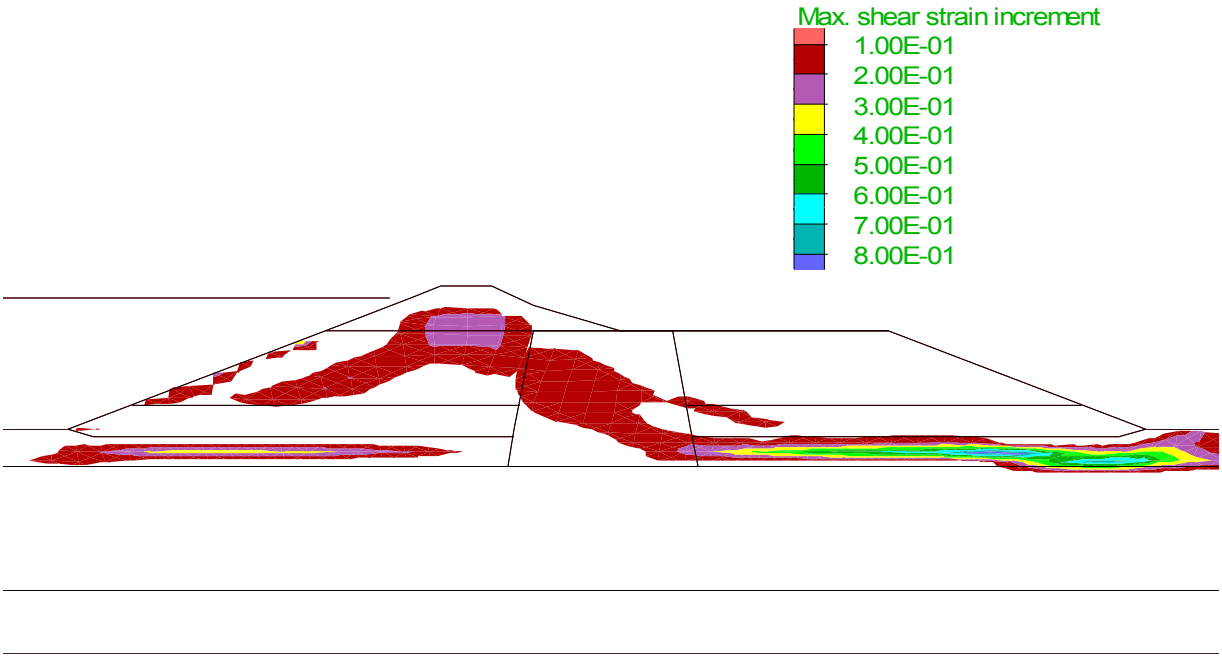

Figure 39. Contours of maximum shear strain at end of post-earthquake analysis (base analysis).

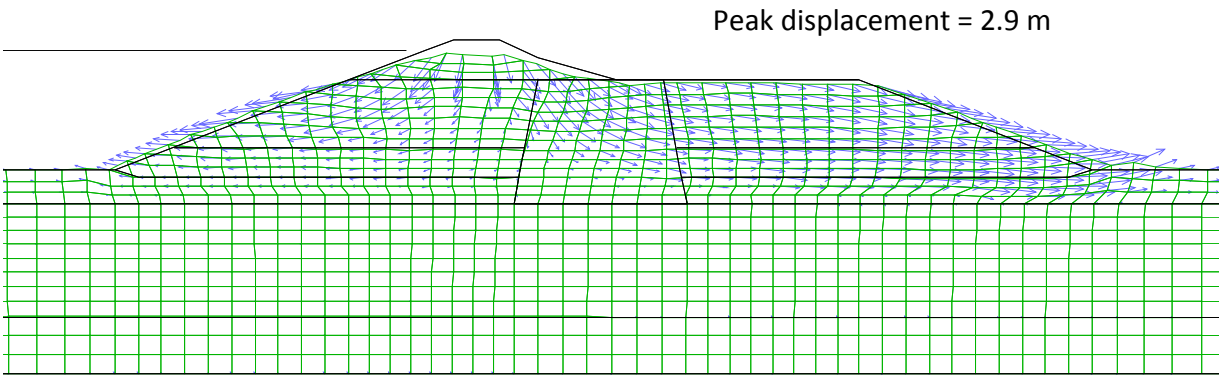

Figure 40. Displaced shape and displacement vectors at end of post-earthquake analysis (base analysis).

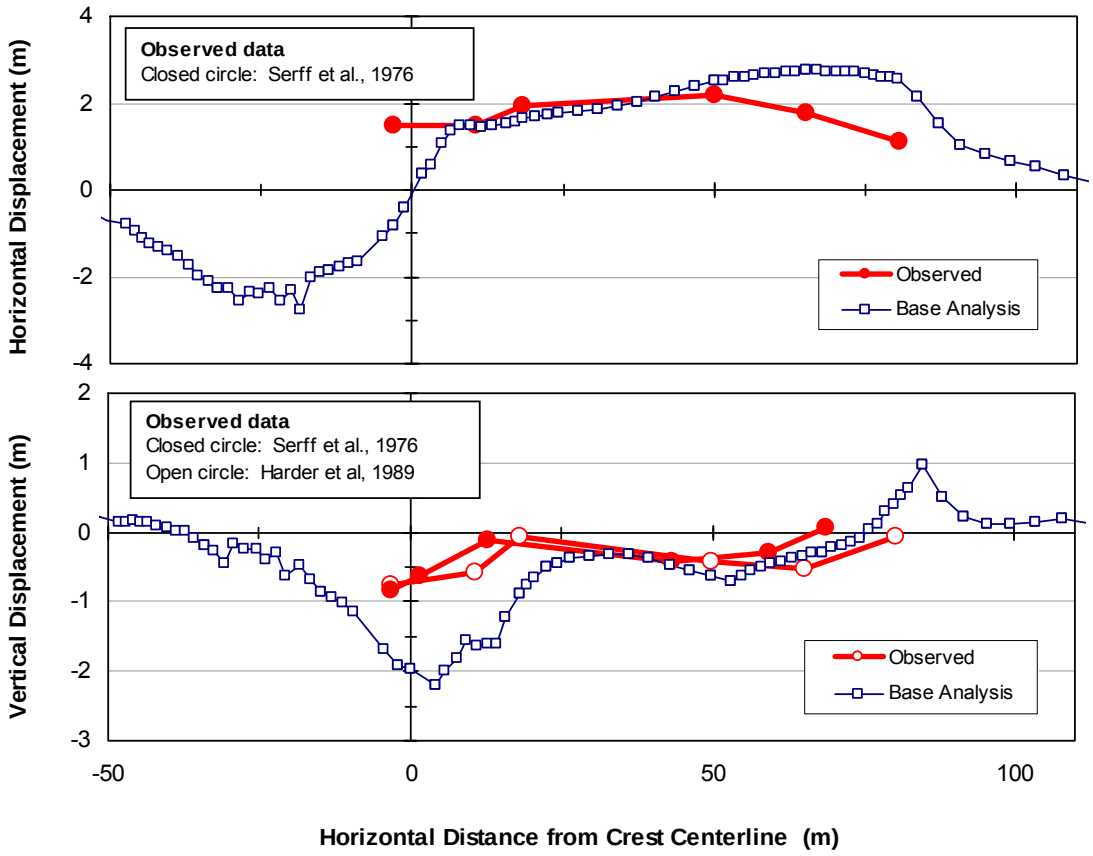

Figure 41. Predicted surface displacements versus observed (Serff, Harder et al 1990).

The base analysis demonstrates that while the 904aR model does not capture all details of the observed response, it does predict displacement behavior that is generally similar in both magnitude and pattern to the observed behavior.

Parametric analysis predictions

Several parametric analyses were performed as described in Table 4. All analyses were identical to the base analysis except as indicated.

Figure 42 presents the predicted surface displacements for Analyses A, B, and C. Analysis A and B show that a reasonable change in the undrained behavior of the core had relatively little impact on the predicted displacements. Analysis C shows that using 33rd percentile estimates of blowcount to characterize the liquefaction resistance of the hydraulic fill produces a modest increase in the predicted deformations.

Figure 43 compares results from the 904a and 904aR models. Two estimates of surface displacement are shown: one at the end of shaking and the second at the end of the post-earthquake analysis. The 904aR model provides a better estimate of the final horizontal displacement magnitudes, although the 904a model is seen to give a better prediction of vertical displacements. The difference between the displacement estimate at the end of shaking and at the end of the post-earthquake analysis is substantial for the 904aR analysis and negligible for the 904a analysis. This change in the relative importance of the post-earthquake analysis is due to the predicted extent of high excess pore pressures below the downstream slope. The peak predicted pore pressure ratios from these two analyses are shown in Figure 44.

Table 4. Summary of parametric analyses, USFD.

Analysis Case	$(N_1)_{60}$ for triggering	S_u / σ'_{vo} for core	Hydraulic Fill Model	Permeability of Hydraulic Fill Shells
Analysis A (base analysis)	median	0.13	904aR	Table 2
Analysis B	median	**0.25 (peak) 0.13 (res)**	904aR	Table 2
Analysis C	**33rd**	0.13	904aR	Table 2
Analysis D	median	0.13	**904a**	Table 2
Analysis E	median	0.13	904aR	**0.10 × Table 2**

Analysis E investigates the influence of the hydraulic conductivity of the hydraulic fill shells. This analysis is the same as the base analysis except the permeability value in the shells has been reduced by a factor of 1/10. Predictions of surface displacement for this case are shown in Figure 45. Reducing the permeability of the shells caused a modest decrease in the predicted displacements at locations downstream of the crest. One possible cause is the reduced ability in Analysis E for high pore pressures to migrate from zones susceptible to liquefaction to zones that are less susceptible. The change in permeability does have some impact on the distribution of peak excess pore pressure, as shown in Figure 44.

These limited parametric studies help to confirm the results obtained from the base analysis by demonstrating only modest variations in the predicted response for analyses using version 904aR. The studies also show the importance of the post-earthquake analysis to the prediction of displacements. In addition, the version 904aR model provides a somewhat better estimate of behavior in this case as compared version 904a.

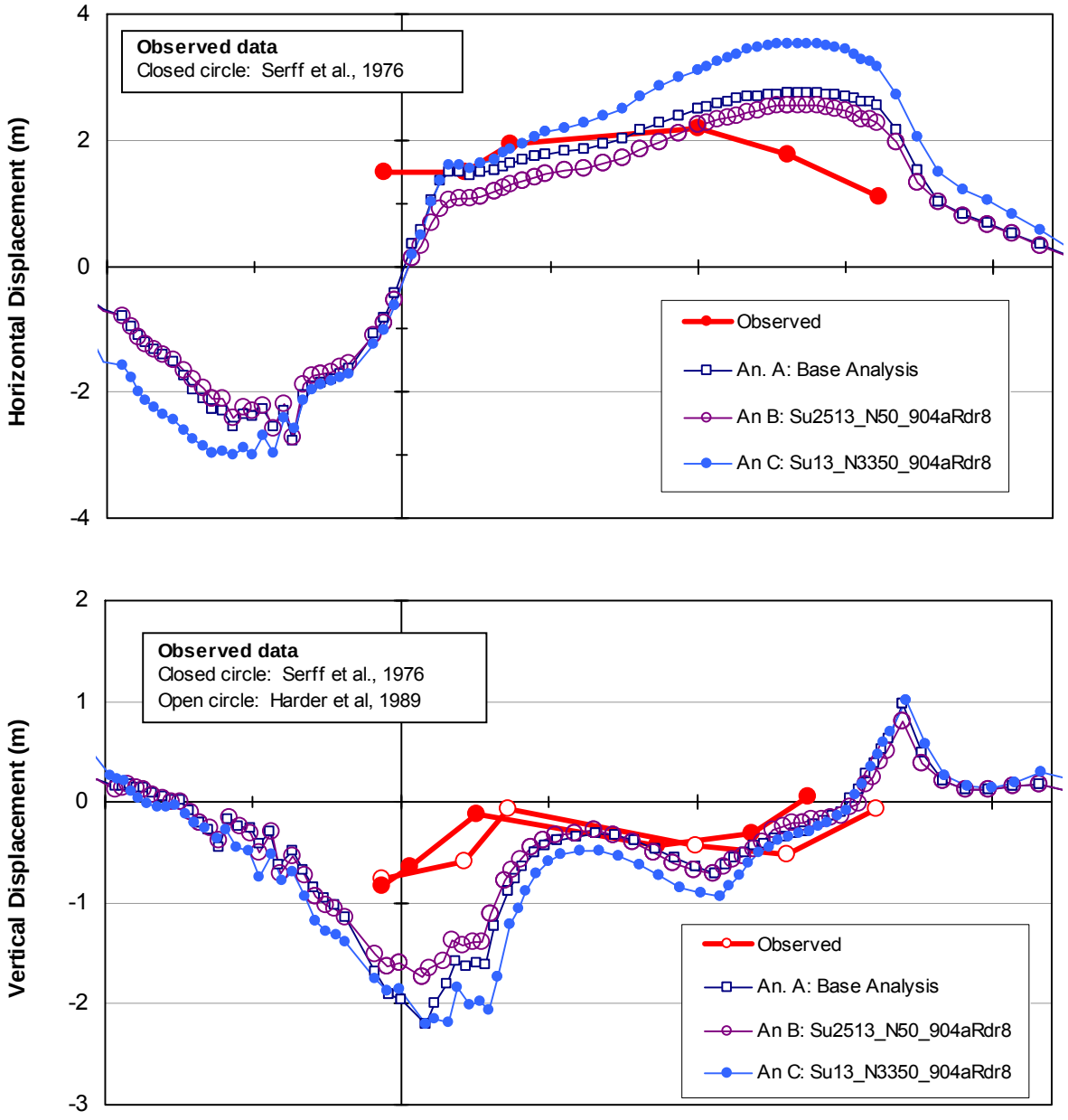

Figure 42. Predicted surface displacements for analyses A, B and C.

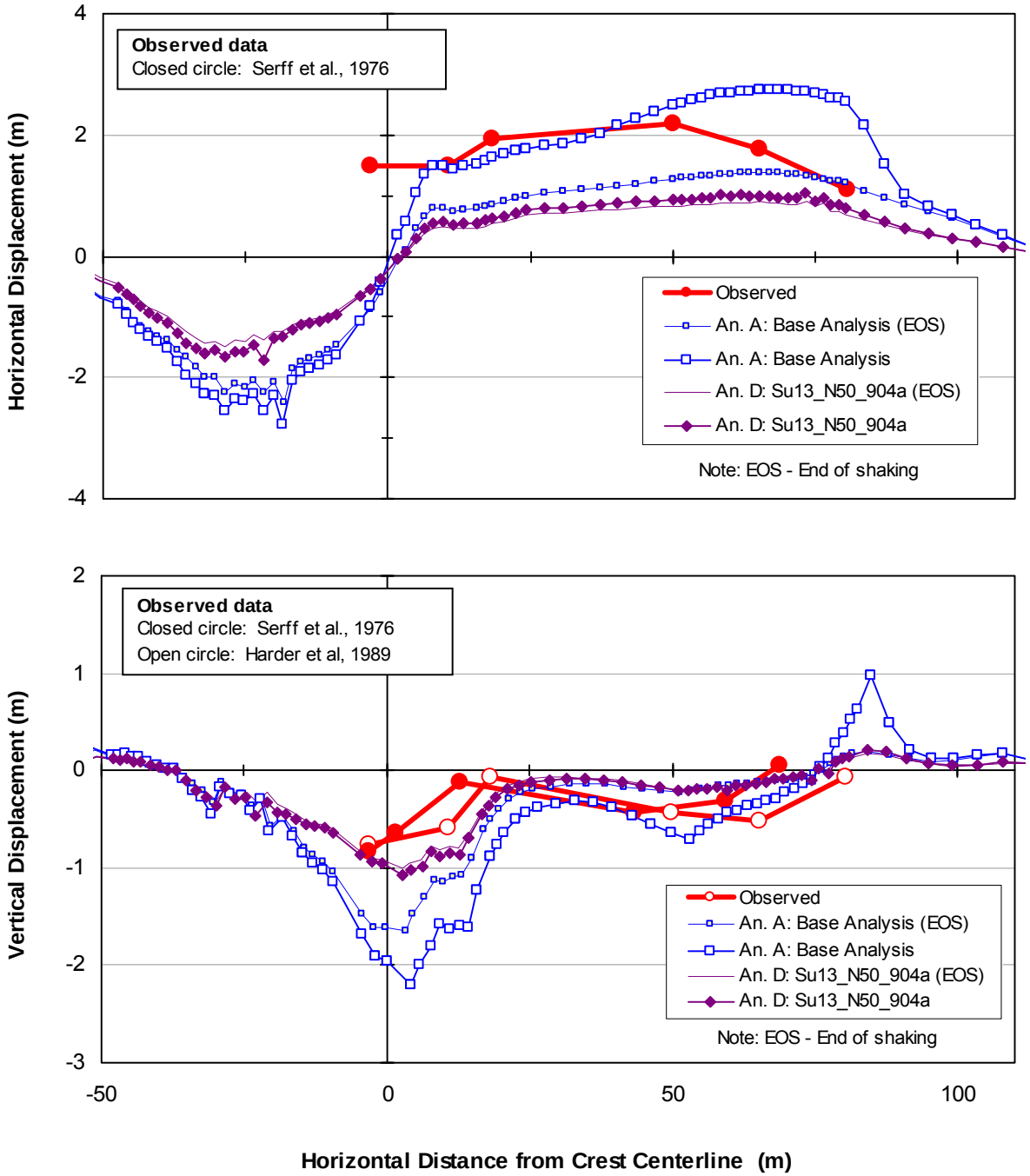

Figure 43. Predicted surface displacements for analyses A and D.

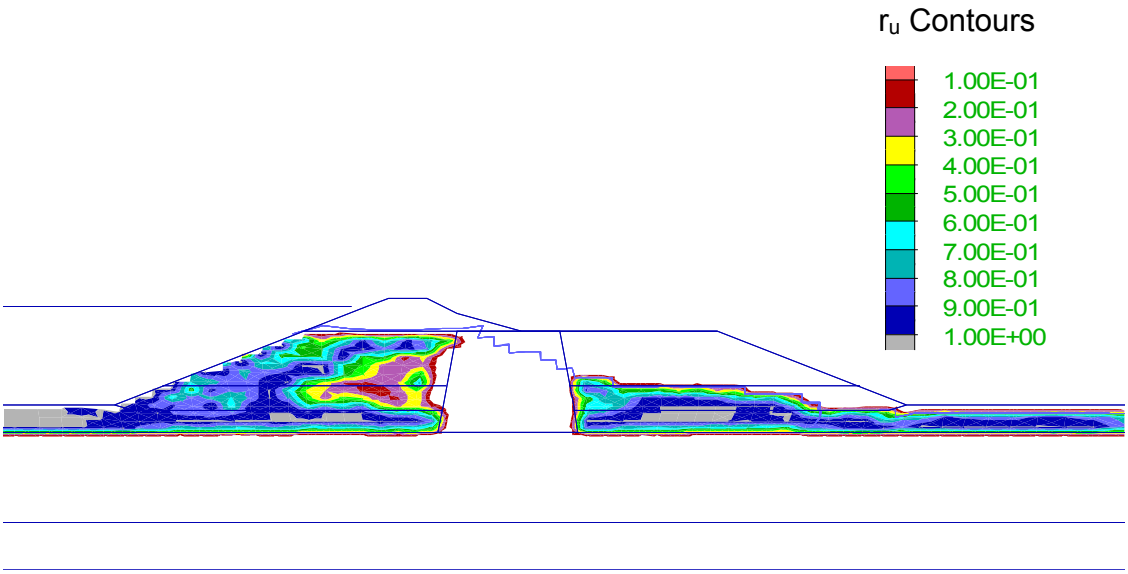

a. Analysis A (version 904aR)

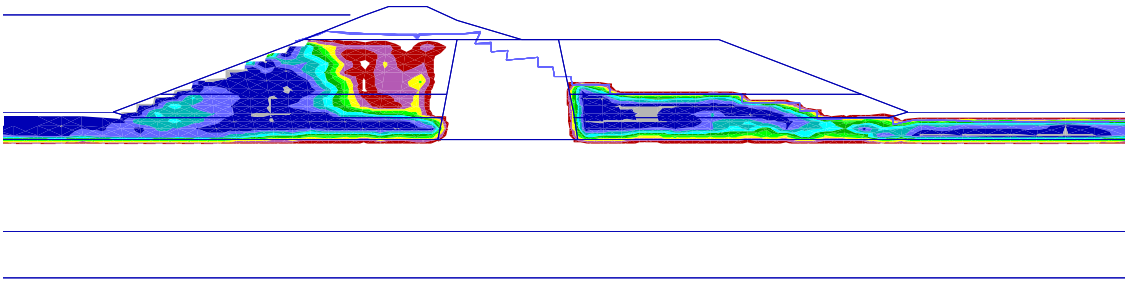

b. Analysis D (version 904a)

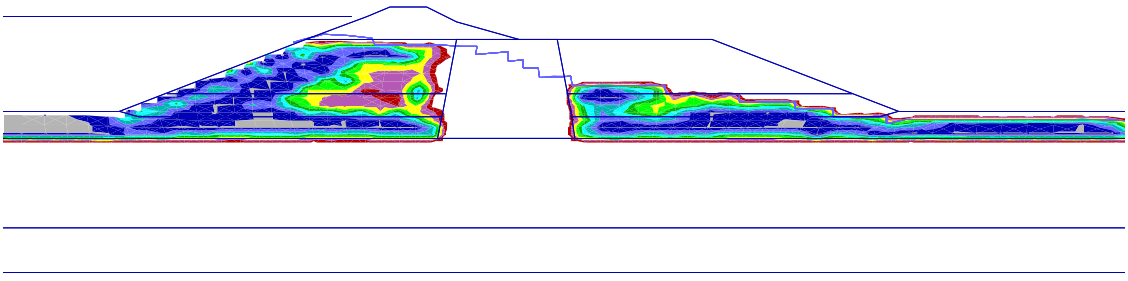

c. Analysis E (version 904aR and reduced shell permeability)

Figure 44. Contours of peak excess pore pressure ratio, r_u, for analyses A, D and E.

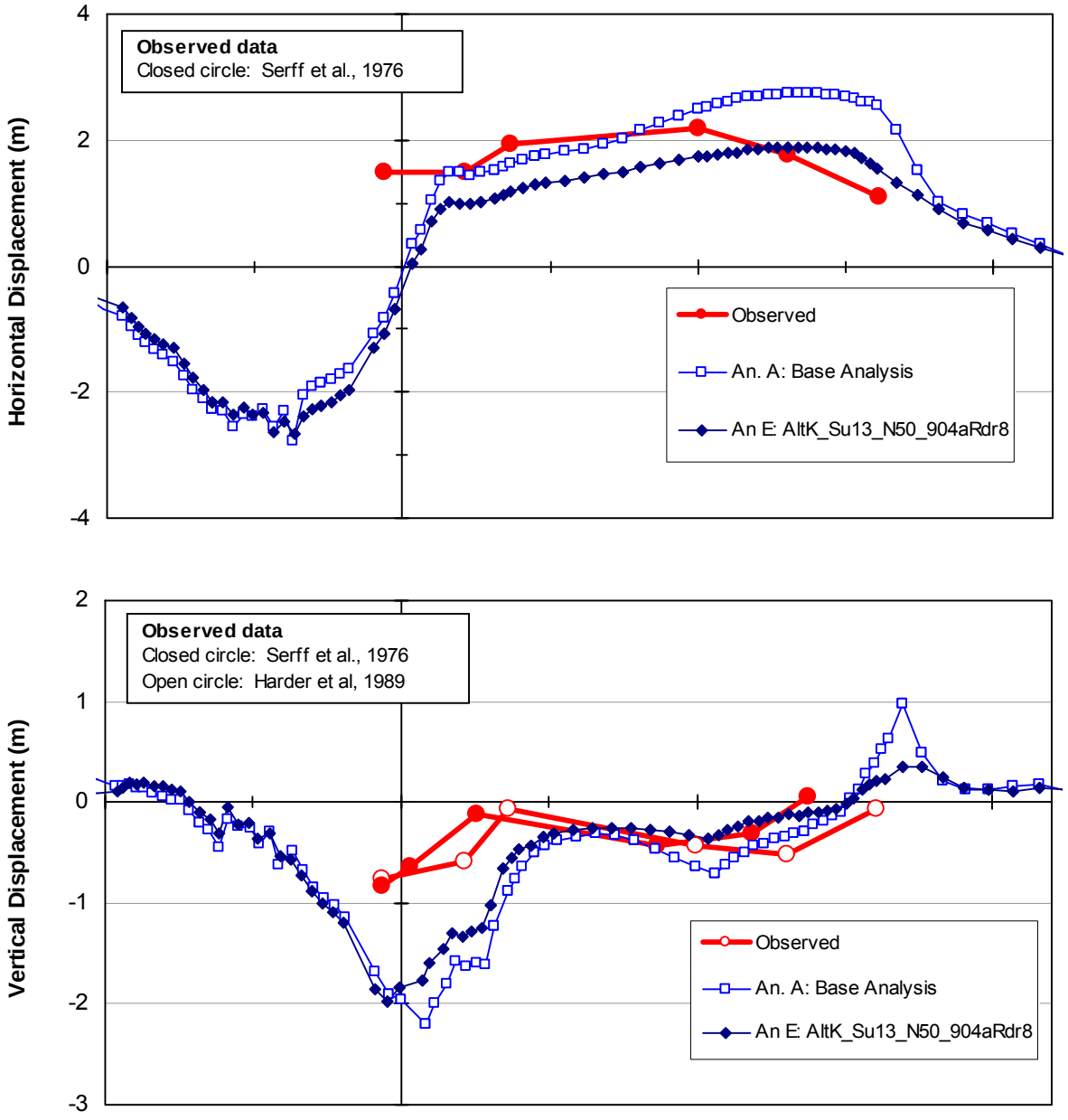

Figure 45. Predicted surface displacements for analyses A and E.

7 References

Aubertin, M., Chapuis, R.P., and Mbonimpa, M. (2005). "Discussion of 'Goodbye, Hazen; Hello, Kozeny-Carman,' by W. David Carrier III," ASCE Journal of Geotechnical and Geoenvironmental Engineering, August.

Bardet, J.P., Davis, C.A. (1996). "Performance of San Fernando Dams during 1994 Northridge Earthquake," ASCE Journal of Geotechnical Engineering, 122(7), 554-564.

Byrne, P.M., Cheung, H., and Yan, L. (1987). "Soil parameters for deformation analysis of sand masses," Canadian Geotechnical Journal, 24(3), 366-376.

Carrier (III), W.D. (2003). "Goodbye, Hazen; Hello, Kozeny-Carman," technical note, ASCE JGGE, 129(11), 1054-1056.

Cetin, K.O. et al. (2004). "Standard Penetration Test-Based Probabilistic and Deterministic Assessment of Seismic Soil Liquefaction Potential," ASCE JGGE 130(12), 1314-1340.

Harder, L.F. Jr., and Boulanger, R.W. (1997) "Application of Kσ and Kα Correction Factors," Proc. of the NCEER Workshop on Evaluation of Liquefaction Resistance of Soils, Report NCEER-97-0022, National Center for Earthquake Engineering Research, SUNY Buffalo, N.Y., pp. 167-190.

Harder, L. F., Hammond, W. D., Driller, M. W., and Hollister, N. (1989). The August 1, 1975 Oroville earthquake investigation, Bulletin 203-88, Calif. Dept. of Water Resources.

Idriss, I.M. (1999). Personal communication.

Idriss, I.M. and Boulanger, R.W. (2006). "Semi-empirical procedures for evaluating liquefaction potential during earthquakes," Soil Dynamics and Earthquake Engineering, 26(2006), 115-130.

Idriss, I.M. and Boulanger, R.W. (2003). "Estimating K_α for use in Evaluating Cyclic Resistance of Sloping Ground," In Proc., Eighth U.S.-Japan Workshop on Earthquake Resistant Design of Lifeline Facilities and Countermeasures Against Liquefaction, Technical Report MCEER-03-0003, Multidisciplinary Center for Earthquake Engineering Research.

Idriss, I. M. and Boulanger, R.W. (2007). "Residual Shear Strength of Liquefied Soils," In Proc., 27th USSD Annual Meeting and Conference, March 2007.

Marcuson, W.F., Hynes, M.E., and Franklin, A.G. (1990). "Evaluation and Use of Residual Strength in Seismic Safety Analysis of Embankment Dams," Earthquake Spectra, Vol 6., No. 3, pp. 529-572.

Martin, G.R., Finn, W.D.L., and Seed, H.B. (1975). "Fundamentals of liquefaction under cyclic loading," Journal of the Geotechnical Engineering Division, ASCE, 101(GT5), pp. 423–438.

Matsuoka, H., and Nakai, T. 1977. "Stress-strain relationship of soil based on the SMP." In Proceedings of the Specialty Session 9, 9th International Conference on Soil Mechanics and Foundation Engineering, pp. 153-162.

Rowe, P.W. 1962. "The stress-dilatancy relation for static equilibrium of an assembly of particles in contact." In Proceedings of the Royal Society of London, Mathematical and Physical Sciences, Series A, 269: 500-557.

Seed, H.B., Martin, P.P. and Lysmer, J. (1976). "Pore-Water Pressure Changes during Soil Liquefaction," Journal of the Geotechnical Engineering Division, ASCE, Vol. 102, No. GT4, pp. 323-346.

Seed, H.B., Lee, K.L., Idriss, I.M., & Makdisi, F. (1973). "Analysis of the Slides in the San Fernando Dams during the Earthquake of Feb. 9, 1971." Report No. EERC 73-2, Earthquake Engineering Research Center, University of California, Berkeley.

Serff, N., Seed, H.B., Makdisi, F.I., and Chang, C.-Y. (1976). "Earthquake Induced Deformations of Earth Dams," Rep. No. EERC 76-4, Univ. of Calif., Berkeley.

Tokimatsu, K. & Seed, H.B. (1987). "Evaluation of Settlements in Sands due to Earthquake Shaking," ASCE Journal of Geotechnical Engineering, 113(8), 861-878.

Youd, T. L., Idriss, I.M., et al. (2001). "Liquefaction resistance of soils: summary report from the 1996 NCEER and 1998 NCEER/NSF workshops on evaluation of liquefaction resistance of soils." J. Geotech. And Geoenvir. Engrg., ASCE, 127(10), 817-833.

8 Appendices

Appendix 1:
Additional references for UBCSAND

Project	Analysis Type	Reference
Sloping ground	Centrifuge prediction	Seid-Karbasi, Byrne, Naesgaard, Park, Wijewickreme, & Phillips (2005)
Sloping ground with silt layers	Centrifuge simulation	Naesgaard, Byrne, Seid-Karbasi, & Park (2005)
Massey Tunnel	Centrifuge simulation	Yang, Naesgaard, Byrne, Adalier, & Abdoun (2004).
High confining stress	Centrifuge simulation	Byrne, Park, Beaty, Sharp, Gonzalez, & Abdoun (2004).
Sloping ground	Centrifuge simulation	Byrne, Park & Beaty (2003)
Mochikochi Dam No. 1	Case history	Byrne and Seid-Karbasi (2003).
Note: Selected papers can be downloaded from http://www.civil.ubc.ca/liquefaction/publications.htm		

References:

Byrne, P.M., Park, S.S., Beaty, M., Sharp, M.K., Gonzalez, L., & Abdoun, T. (2004). "Numerical modeling of liquefaction and comparison with centrifuge tests," Canadian Geotechnical Journal, Vol. 41(2):193-211.

Byrne, P.M., Park, S.S. & Beaty, M. (2003). "Seismic liquefaction: centrifuge and numerical modeling," in Proc., 3rd International FLAC Symposium, Sudbury, October.

Byrne, P.M. & Seid-Karbasi, M. (2003). "Seismic stability of impoundments," 17th Annual Symposium, Vancouver Geotechnical Society, Vancouver, B.C.

Naesgaard, E., Byrne, P.M., Seid-Karbasi, M. & Park, S.S. (2005). "Modeling flow liquefaction, its mitigation, and comparison with centrifuge tests," Geotechnical Earthquake Engineering Satellite Conference, Osaka, Japan

Seid-Karbasi, M., Byrne, P.M., Naesgaard, E., Park, S.S., Wijewickreme, D. & Phillips, R. (2005). "Response of Sloping Ground with Liquefiable Materials During an Earthquake: A Class A Prediction," in Proceedings, 11th International Conference, International Association for Computer Methods and Advances in Geomechanics, Italy.

Yang, D., Naesgaard, E., Byrne, P.M., Adalier, K. & Abdoun, T. (2004). "Numerical model verification and calibration of George Massey Tunnel using centrifuge models," Canadian Geotechnical Journal 41(5): 921-942.

Other References:

Beaty, M. & Byrne, P.M. (1998). An effective stress model for predicting liquefaction behaviour of sand. In P. Dakoulas, M. Yegian, & R. D. Holtz (Eds.), Geotechnical Earthquake Engineering and Soil Dynamics III, ASCE Geotechnical Special Publication No. 75, Vol. 1, Proceedings of a Specialty Conference (pp. 766-777). Seattle: ASCE.

Puebla, H., Byrne, P.M., & Phillips, R. (1997). Analysis of CANLEX Liquefaction Embankments: Prototype and Centrifuge Models. Canadian Geotechnical Journal, 34(5), 641-657.

Appendix 2:
Generic input parameters for UBCSAND 904aR

```
water bulk    =         ; Generic input parameters assumed fmod = 5e5 kPa
prop m_n160   =         ; Assign appropriate value of (N1)60cs
prop m_pa     =         ; Assign value of atmospheric pressure in model units
prop m_phicv  = 33.
prop porosity = 0.5
def properties
 loop i (1,izones)
 loop j (1,jzones)
 ;ELASTIC
   $N160 = z_prop(i,j,'m_n160')
   z_prop(i,j,'m_kge')  = 21.7*20.* $N160^.333  ;Shear Mod
   z_prop(i,j,'m_kb')   = z_prop(i,j,'m_kge')*.7              ;Bulk mod
   z_prop(i,j,'m_me')   = 0.5
   z_prop(i,j,'m_ne')   = 0.5
;
 ;PLASTIC PROPERTIES
   z_prop(i,j,'m_kgp')  = z_prop(i,j,'m_kge')* $N160 ^2*.003 +100.0  ;shear Mod
   z_prop(i,j,'m_np')   = .4
   z_prop(i,j,'m_phif') = z_prop(i,j,'m_phicv') + $N160 /10.0
   z_prop(i,j,'m_phif') = z_prop(i,j,'m_phif')  + max(0.0,( $N160 -15.)/5.)
;
 ;plastic modification factors
   z_prop(i,j,'m_hfac2') = 1.0  ;Secondary hardener
   z_prop(i,j,'m_hfac3') = 1.0  ;dilation "hardener"
   ;   m_hfac1 = a(N) * (Sigvo'/Patm)^b(N)
   ;   where
   ;   a(N)   = 1.05 -0.03*N +0.004*N^2 -0.000185*N^3 +2.92e-6*N^4
   ;   b(N)   = 1./(-0.424 -0.259*N +0.00763*N^2)
   $a_N   = 1.05 -0.03*$N160 +0.004*$N160 ^2
   $a_N   = $a_N -0.000185*$N160 ^3 +2.92e-6*$N160 ^4
   $b_N   = 1./(-0.424 -0.259*$N160 +0.00763*$N160 ^2)
   $SigP  = max((-syy(i,j)-pp(i,j))/ z_prop(i,j,'m_pa'),1.0)
   z_prop(i,j,'m_hfac1') = $a_N * ($SigP)^$b_N
;
 ;failure ratio --same as in Hyperbolic model
   z_prop(i,j,'m_rf') = 1.1*$N160 ^(-0.15)
   z_prop(i,j,'m_rf') = min(z_prop(i,j,'m_rf'),.99)
;
 ;plastic anisotrophy
   z_prop(i,j,'m_anisofac') = 1.0    ; Generic parameters do not address anisotropy
   z_prop(i,j,'m_static')   = 1.0        ; = 1.0 for initial static setup;   = 0.0 for
dynamic
 end_loop
 end_loop
end
```